Journal of Microelectronics and Electronic Packaging (2015) **12**, 1-28

ISSN: 1551-4897

Manufacturability and Reliability Screening of Lower Melting Point, Pb-Free Alloys Containing Bismuth

Joseph M. Juarez Jr.,[1] Polina Snugovsky,[2,*] Eva Kosiba,[2] Zohreh Bagheri,[2] Subramaniam Suthakaran,[2] Michael Robinson,[1] Joel Heebink,[1] Jeffrey Kennedy,[2] and Marianne Romansky[2]

Abstract—**This paper explores the manufacturability and reliability of three Pb-free Bi-containing alloys in comparison with conventional SAC305 and SnPb assemblies. The first alloy included in the study is a Sn-based alloy with 3.4%Ag and 4.8%Bi, which showed promising results in the National Center for Manufacturing Sciences and German Joint projects. The other two alloy variations have reduced Ag content, with and without Cu. BGA and leaded components were assembled on medium-complexity test vehicles using these alloys, as well as SAC305 and SnPb as baseline alloys, for comparison. Test vehicles were manufactured using two board materials, 170°C glass transition temperature (T_g) and 155°C T_g, with three surface finishes: ENIG, ENEPIG, and OSP. The accelerated temperature cycling (ATC) testing was done at −55°C to 125°C with 30-min dwells and 10°C/min ramps, for 3,000 cycles. Detailed microstructure examination before and after ATC testing is described, as is failure analysis. All three experimental alloys showed excellent performance in harsh-environment thermal cycling. Vibration testing at two G-force test conditions with resistance failure monitoring was performed on the daisy-chained components. A detailed description of the technique for the vibration testing using 2 G and 5 G harmonic dwells is provided. The lowest failure rate found at both the 2 G and 5 G levels was for the Cu-containing alloy known as Violet. These results provide data for further statistical analysis leading to the choice of proper combinations of the solder alloys, board materials, and surface finishes for high-reliability applications.**

Introduction

Aerospace and military companies continue to exercise Restriction of Hazardous Substances (RoHS) regulation exemptions and to intensively research the long-term attachment reliability of RoHS-compliant solders. Their products require higher vibration, drop/shock performance, and combined-environment reliability than the conventional SAC305 alloy provides. The National Aeronautics and Space Administration–US Department of Defense (NASA–DoD) Lead-Free Electronics Project confirmed that pad cratering is one of the dominant failure modes that occur in various board-level reliability tests, especially under dynamic loading [1].

The manuscript was received on September 10, 2014; revision received on January 5, 2015; accepted on January 6, 2015

The original version of this paper was presented at IPC APEX'2013 (first part) and IPC APEX'2014 (second part).

[1]Honeywell International Inc., Phoenix, Arizona

[2]Celestica Inc., Toronto, ON, Canada

*Corresponding author; email: polina@celestica.com

One possible route to improvement of the mechanical and thermomechanical properties of solder joints is the use of Pb-free solders with lower process temperatures. Lower temperatures help reduce the possibility of damaging the boards and components, and also may allow for the use of relatively lower glass transition temperature (T_g) board materials, which are less prone to pad-cratering defects. There are several SnAgBi and SnAgCuBi alloys that melt at a temperature about 10°C lower than the melting temperature of SAC305. The bismuth in these solder compositions not only reduces the melting temperature, but also improves thermomechanical behavior [2-4]. An additional benefit of using Bi-containing solder alloys is the reduction in the propensity to whisker growth [5]. Alloys containing Bi have not been widely utilized, due to the formation of a low melting ternary SnPbBi alloy when SnAgCuBi solder joints are contaminated with Pb from SnPb component finishes. With the increased use of Pb-free solder alloys and component finishes, SnPb component finishes are becoming obsolete, reducing the risk of Pb contamination of Bi-containing solder alloys.

Several ternary SnAgBi and quaternary SnAgCuBi Pb-free solder alloys have shown great mechanical and thermomechanical reliability in previously completed projects—the National Center for Manufacturing Sciences (NCMS) [6] and Joint Council on Aging Aircraft/Joint Group on Pollution Prevention Lead-Free Solder Project [7]—and new studies (German Joint Project (GJP) Lead-Free Avionics) recently presented at the Aerospace Industry Association PERM meeting [8]. Some of these Pb-free alloys have melting temperatures comparable to SnPb, allowing the use of SnPb processing temperatures for Pb-free assemblies. Some alloys may have a lower Ag content that will reduce the solder cost and contribute to mechanical property improvements.

Celestica, in a partnership with the University of Toronto, has been working since 2009 on a project with the objective of selecting new Pb-free alloys with process temperatures comparable to conventional SnPb solder for assembly and rework of ball grid array (BGA), leaded, and pin-through-hole components [9]. From an initial list of 23 alloys studied for metallurgical performance, a total of seven SnAgBi and SnAgCuBi alloys selected for screening experiments of mechanical and thermomechanical properties showed good manufacturability and drop-test performance.

This paper explores the manufacturability and reliability screening results for three Bi-containing alloys in comparison with conventional SAC305 and SnPb assemblies.

doi:10.4071/imaps.441

Experiments

The extensive Experiments section of this paper includes descriptions of the alloy matrix, test vehicle details, assembly processes, metallurgical analysis, and accelerated thermal-cycling parameters and procedures. An extensive explanation of vibration test techniques and data collection protocols for strain and resistance monitoring during mechanical stress testing is also provided.

A. Alloy Selection

Three of seven alloys analyzed in the Celestica–University of Toronto study [9] were selected for the high-reliability environment testing. The alloy names, constituent elements, minimum melting temperatures, and melting temperature ranges are shown in Table I.

- Alloy 1, proposed by Paul Vianco, is labeled "Paul." This alloy's excellent thermomechanical properties for harsh environments have been proven by NCMS [6] and the German Joint Lead-Free Avionics project [8]. Alloys 2 and 3 are modifications of the Paul alloy.
- Alloy 2, "Violet," has a lower Ag content and does not form Ag_3Sn plates, the absence of which may help improve drop/shock properties. Cu is added to the formulation to reduce the Cu dissolution potential. The increased Bi content related to the reduced Ag may help better mitigate whisker formation and slightly lower the melting temperature compared with the Paul alloy. Both alloys have an excellent pasty range [10].
- Alloy 3, "Orchid," is a variant of the Paul alloy, with a lower Ag and higher Bi content than both Paul and Violet, which allows the significant reduction of the minimum melting temperature. The pasty range is wider than in alloys 1 and 2. Because of a lower melting temperature and higher Bi content, it may dissolve even less Cu and provide greater whisker mitigation than Paul [10].

SAC305 and SnPb solders are included in the test matrix for baseline comparisons. No-clean solder pastes of the experimental alloys were produced by one of the major solder-paste suppliers. The solder-paste performance evaluation was done using a Celestica test vehicle and a standard Celestica solder-paste evaluation procedure [11].

B. Test Vehicle

The board stack up and dimensions of the test vehicle are representative of a large percentage of aerospace products and designed per IPC-4101/126 and /129 requirements. Assembling this well-characterized board in a variety of board finishes while processing duplicate sets of components should make the comparison of various low-melt Pb-free alloys easier. The assembly and reflow processes have been optimized to accommodate the assembly of various daisy-chained SAC305, BGA, and matte Sn leaded components.

1) Board Materials

The objective of testing different laminate materials is to evaluate the pad-cratering benefit obtained when using a lower T_g material enabled by the lower process temperature achievable with the experimental alloys. This lower T_g, in combination with the lower process temperature, is expected to deliver equal or better performance at a potentially lower cost point. "Lower T_g" is used as a relative descriptor in this paper, and refers to a 155°C T_g laminate material, which is becoming the new "normal" T_g laminate, and softens at a lower temperature than the "high T_g" laminate. The "high T_g" laminate refers to a 170°C T_g laminate material. The 155°C T_g laminate material used was Nelco 4000-7, and the 170° C T_g laminate was Isola 370HR.

2) Board Surface Finishes

Multiple surface finishes are used to compare soldering performance at various metallic interfaces and to review reliability performance when soldered to copper or nickel. The OSP used was a copper triazole. The ENIG finish had a Ni thickness of 3.81 μm and Au thickness of 0.13-0.20 μm. The ENEPIG finish also had a Ni thickness of 3.81 μm, Pd thickness of 0.05 μm, and Au thickness of 0.08 μm.

3) Dimensions and Number of Layers

The overall dimensions for the PWB test vehicle were approximately 203 mm × 355 mm and 2.5 mm thick, with 16 layers of alternating copper signal and ground/power planes. All of the wiring on the PWB is to accommodate daisy-chain, active-resistance monitoring and output to an edge connector pattern for wiring. Fig. 1 illustrates the test vehicle, which includes packages representative of the variety typically seen on products.

The package types, component dimensions, I/O counts, solder ball composition, and lead finishes are shown in Table II.

These partially assembled boards were continuously monitored with Anatech (Analysis Tech Inc.) resistance-event detection equipment during harsh-environment accelerated thermal cycling and vibration exposures representative of product

Table I
Alloys Selected for High-Reliability Screening Experiments

#	Celestica name	Alloy constituents	Alloy composition, %	Minimum melting temperatures, °C (Experimental)	Melting range, °C
1	Paul	SnAgBi	Sn3.4Ag4.8Bi	206	11
2	Violet	SnAgCuBi	Sn2.25Ag0.5Cu6.0Bi	205	10
3	Orchid	SnAgBi	Sn2.0Ag7.0Bi	190	25
4	SAC305	SnAgCu	Sn3.0Ag0.5Cu	217	6
5	SnPb	SnPb	Sn37.0Pb	183	0

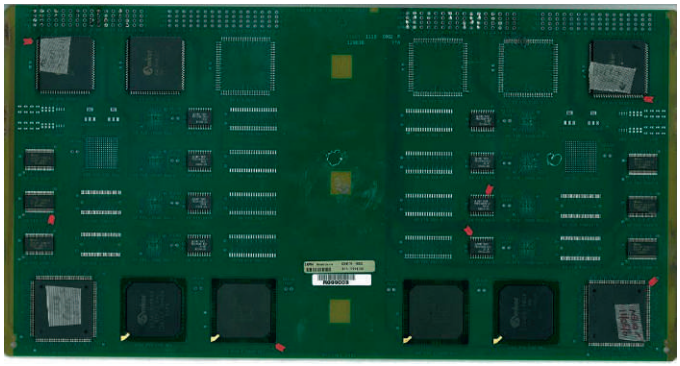

Fig. 1. Test vehicle.

Table II
Component Types

I/O count	Package	Dimensions, mm	Pitch, mm	Lead finish	Ball composition
20	SO	6.35 × 12.70	1.27	SnPb and Matte Tin	
40	SOJ	10.16 × 25.40	1.27	SnPb and Matte Tin	
48	SOP	5.08 × 15.24	0.50	SnPb and Matte Tin	
54	TSSOP	10.16 × 21.59	0.64	SnPb and Matte Tin	
84	PLCC	29.21 × 29.21	1.27	SnPb and Matte Tin	
240	PQFP	31.75 × 31.75	0.50	SnPb and Matte Tin	
289	BGA	17.15 × 17.15	1.02		SnPb and SAC305
352	BGA	35.56 × 35.56	1.27		SnPb and SAC305
1,156	BGA	34.93 × 34.93	1.02		SnPb and SAC305

requirements. The range of component type, size, and board finishes provided a comprehensive look at selected lower-melt Pb-free alloys that could be compared with SAC 305 and SnPb baseline test data.

This screening experiment defines the critical variables and provides a path for more in-depth industry studies of low-melt solders, while minimizing the costs.

C. Assembly

Fifty-six of the test vehicles were built at Celestica using different combinations of board material, surface finish, and alloys, as outlined in Table III.

Seven thermocouples were placed on test vehicle assemblies at various locations, both on components and on the board itself, to determine the optimal profiles. Two profiles were used, one with a peak reflow temperature of 240°C for SAC305 and one with a peak reflow of 222°C for all other alloys. In both cases, the time above liquidus was between 70 and 90 s. The profiles are shown in Fig. 2 and Fig. 3, respectively. All boards were reflowed in a 10-zone Electrovert Omniflow oven.

During the solder screening process, solder paste heights and volumes were measured. Every attempt was made to print equal volumes of the various solder pastes. All components were placed using a Siemens Siplace X3 SMT placement machine with a standard nozzle. Visual and radiographic inspections were then performed on each of the assembled boards. Additionally, one assembly was sent for cross-sectioning to ensure the appropriateness of the profiles prior to completion of the build.

Table III
Build Matrix

Board material	Alloy	Surface finish: ENEPIG	ENIG	OSP
"Normal" T_g 155°C	SnPb	2	. . .	3
	SAC305	2	. . .	2
	Paul	. . .	. . .	4
	Violet	. . .	4	. . .
	Orchid	4	. . .	. . .
High T_g 170°C	SnPb	2	. . .	3
	SAC305	2	1	3
	Paul	4	4	. . .
	Violet	4	. . .	4
	Orchid	. . .	4	4

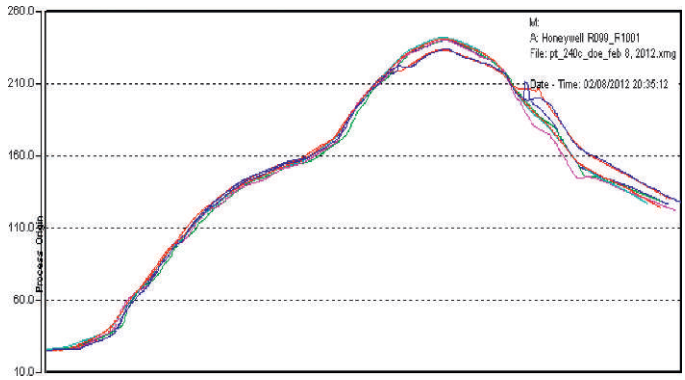

Fig. 2. Reflow profile for 240°C.

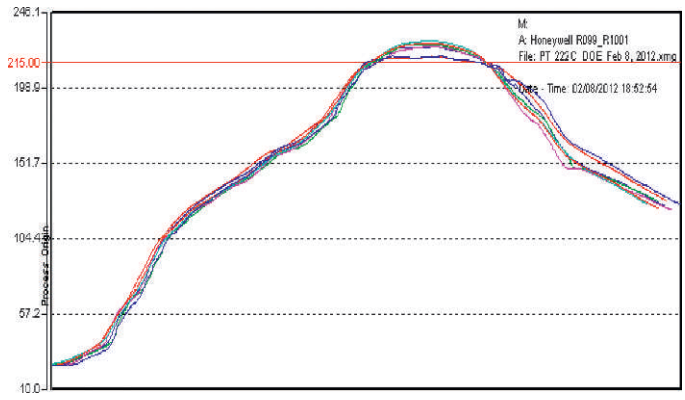

Fig. 3. Reflow profile for 222°C.

D. Metallurgical Analysis After Assembly, and Failure Analysis

Optical microscopy, radiography (Phoenix PCB analyzer), scanning electron microscopy (Hitachi S-4500 and SEM

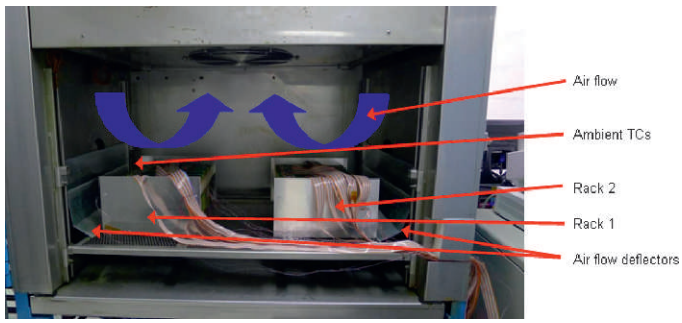

Fig. 4. ATC chamber set up.

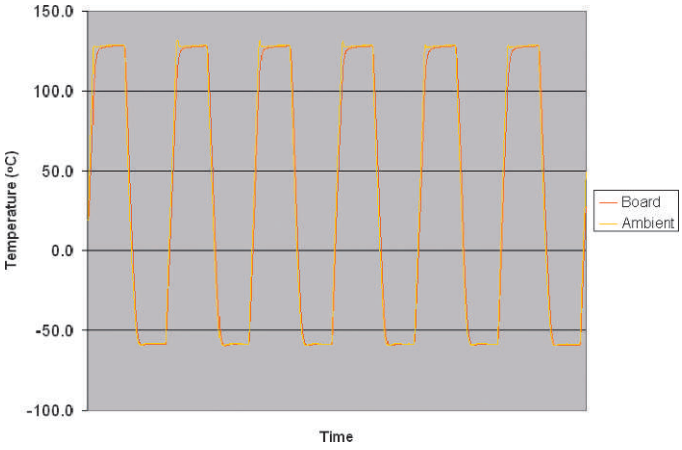

Fig. 5. ATC chamber profile.

Hitachi S-3000N), and x-ray spectroscopy (Oxford EDX) were used for solder-joint quality and microstructure analysis.

BGA352 location U200 was exposed to the lowest temperature during reflow, and QFP240 location U23, which experienced the hottest temperature, were cross-sectioned to analyze the microstructure and measure the intermetallic reaction layer. For the lower melting temperature alloy profile, the lowest temperature of the center and the corner balls of the BGAs was 224.9°C and 227.5°C, respectively. The BGA cross-sectioning was done diagonally. The peak temperature on the quad flat packages (QFPs) was 232°C. Twelve boards were cross-sectioned and analyzed.

E. Accelerated Temperature Cycling

Seventeen test vehicles were exposed to accelerated temperature cycling (ATC). ATC was performed to a target range of −55°C to 125°C, with a ramp rate of 10°C/min and a 30-min dwell at each extreme. The assemblies were placed into two racks within the chamber, as seen in Fig. 4, to allow the air to circulate freely. Temperature measurements for guiding the profile were measured at the test vehicle level (not the chamber level). The actual profile resulted in a hot dwell at 130°C for 38 min and a cold dwell at −58°C for 39 min with a 13-min ramp in between, totaling 103 min/cycle, as shown in Fig. 5. A total of 3,010 cycles were completed before testing was terminated.

Analysis Tech STD-256 event detectors were used to monitor the resistance thresholds of 32 components on each board. A failure was recorded when the channel resistance increased to 300 Ω or more for at least 200 ns. Periodically, the chamber was stopped and the failures recorded by the event detector were removed and electrically probed at room temperature to determine the location of the failure. If the failure was determined to be in a solder joint, rather than in the cabling system or a trace failure within the board, the component was cut out for detailed analysis before the test vehicle was returned to the chamber and temperature cycling resumed.

F. Statistical Considerations for Vibration Testing

To compare the several combinations of solder paste, substrate finish, and T_g, two design experimental matrices were chosen: full factorial, as shown in Table IV, and a Latin square as illustrated in Table V and Table VI.

Specifically, the Latin square design of order three is shown. In general, the rows represent levels of one factor; the columns, another factor; and numbers in the cells, levels of a third factor. The Latin square is a subset of all possible combinations where each level of one factor is present with each level of another factor. The advantage is that the Latin square provides estimates of factor level differences in a fraction of the possible combinations. In this case, the Latin square of order 3 uses nine combinations rather than the 27 required for a full factorial experiment [12].

The T_g factor only has two levels of interest, so the high level was duplicated as the middle level. This is a common

Table IV
Experimental Design Using Three Factors Applied to the Failure of Six Components, Using a Latin Square for Run Combinations 1-9 and a Full Factorial for Runs 10-17

	Paul			Violet			Orchid			SAC305				Sn-Pb			
Paste type Finish	OSP	ENIG	ENEPIG	OSP	ENIG	ENEPIG	OSP	ENIG	ENEPIG	OSP	OSP	ENEPIG	ENEPIG	OSP	OSP	ENEPIG	ENEPIG
T_g, °C	155	170	170	170	155	170	170	170	155	155	170	155	170	155	170	155	170
Run #	1	2	3	4	5	6	7	8	9	10	11	12	13	14	15	16	17
Component Type																	
BGA352	/02	/02	/02	/02	/02	/02	/02	/02	/02	/02	/02	/02	/02	/02	/02	/02	/02
QFP240	/02	/02	/02	/02	/02	/02	/02	/02	/02	/02	/02	/02	/02	/02	/02	/02	/02
SSOP48	/06	/06	/06	/06	/06	/06	/06	/06	/06	/06	/06	/06	/06	/06	/06	/06	/06
PLCC84	/06	/06	/06	/06	/06	/06	/06	/06	/06	/06	/06	/06	/06	/06	/06	/06	/06
SO20	/08	/08	/08	/08	/08	/08	/08	/08	/08	/08	/08	/08	/08	/08	/08	/08	/08
SOJ40	/08	/08	/08	/08	/08	/08	/08	/08	/08	/08	/08	/08	/08	/08	/08	/08	/08

Table V
General Latin Square

	a	b	c
A	1	2	3
B	3	1	2
C	2	3	1

Table VI
Latin Square of Paste and Finish

	Finish		
Paste	OSP	ENIG	ENEPIG
Paul	155	170	170
Violet	170	155	170
Orchid	170	170	155

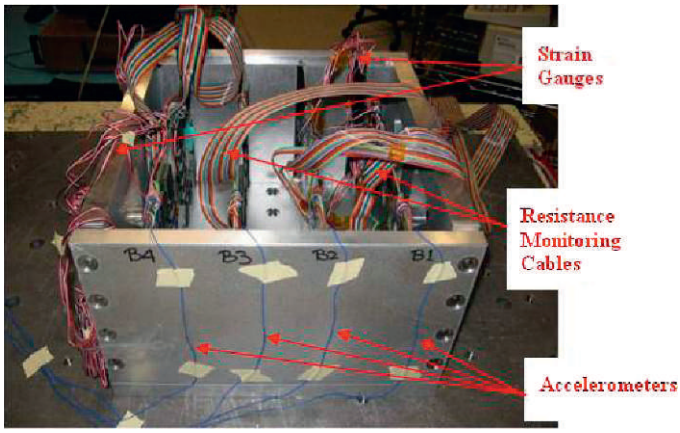

Fig. 6. Vibration fixture with boards.

practice when one factor has fewer levels than the other two, and presents only a minor complication in the analysis. Essentially, the difference between the high and middle levels is known to be equal to zero.

The factorial portion uses factors relevant to the traditional Sn-Pb pastes. In this case, each factor only had two levels of interest, so the traditional 2×2×2 layout was used.

The run data are summarized as pass/fail, with all components combined. The resulting response is proportion, $p = x/n$, of n samples that are defective. This is modeled using the binomial distribution. Unfortunately, this response is known to exhibit the complication of nonconstant variance across inference space. The proportions are transformed using the Freeman-Tukey adaptation of the arcsine of the proportion to stabilize the variance across the treatment combinations. Then, the usual analysis of variance may be used to evaluate factor and level effects.

G. Vibration Testing Overview

Twenty-six test vehicles were subjected to vibration testing, 17 at a 5-G level and nine at a 2-G level. Resistance, strain, and vibration data were recorded. Component failure was determined through resistance monitoring, using the same method described in the ATC testing section. Strain was monitored at regular intervals throughout the test on a representative sample size of boards. Vibration was monitored using an accelerometer at the center of each board, the area that would experience the most flexure. Fig. 6 shows four boards installed in the fixture with the various monitoring systems.

Boards of the same material and similar finish/alloy combinations were grouped for testing, as shown in Table VII. The 26 cards were divided into eight testing groups. All groups were assigned to 2-G and / or 5-G sweeps: Groups 1 through 5 had a 5-G dwell; groups 6 through 8 were assigned to a 2-G dwell. Since only boards used for 5-G testing had strain gauges attached, these boards were exposed to sine sweeps at both 2 G and 5 G to characterize the boards.

H. Vibration Test Procedure and Techniques

1) Fixture

An aluminum fixture was built to hold a maximum of four cards. The fixture has eight wedge locks with special locking mechanisms to secure the cards and ensure samples do not touch the base of the fixture. A sine sweep fixture survey to ensure no resonance occurred within the test frequency range

Table VII
Vibration Test and T_g/Alloy/Finish Parameters per Group

		Fixture location			
Vibration level	Group	B1[a]	B2[a]	B3[a]	B4[a]
5 G	1	170/Violet/ENEPIG[b]	170/Paul/ENIG	170/SAC305/ENEPIG	170/SnPb/ENEPIG
	2	170/Paul/ENEPIG[c]	170/SnPb/OSP	. . .	. . .
	3	170/Orchid/ENIG[b]	170/Violet/OSP	170/SAC305/OSP	170/Orchid/OSP[b]
	4	155/Orchid/ENIG[b]	155/SAC305/OSP	155/SnPb/OSP	. . .
	5	155/Violet/ENIG[c]	155/SAC305/ENEPIG	155/SnPb/ENEPIG	155/Orchid/ENEPIG[c]
2 G	6	155/Paul/OSP	155/Violet/ENIG	155/Orchid/ENEPIG	. . .
	7	170/Paul/ENIG	170/Violet/ENEPIG	170/Orchid/OSP	. . .
	8	170/Paul/ENEPIG	170/Violet/OSP	170/Orchid/ENIG	. . .

[a]Data given as T_g °C/alloy/finish.
[b]Strain gauge scenario 1 used as shown in Fig. 8.
[c]Strain gauge scenario 2 used as shown in Fig. 9.

was conducted. The accelerometer closest to the table was chosen as the control accelerometer. Six accelerometers were used as auxiliary accelerometers to monitor the response of the fixture during the survey. The fixture resonance occurs above 700 Hz; this is well above the testing frequency of 10-200 Hz and provides enough guard bands so that the fixture will not be a factor in the assembly performance results, where the card resonance occurred in the range of 45-68 Hz.

2) Vibration Testing

A 12,000-pound force (53.4 kN) capacity, LDS electrodynamics shaker with a Spectral Dynamics Jaguar controller was used for the vibration testing. The input control accelerometer was mounted on the fixture. The vibration direction was perpendicular to the plane of the boards. Each board's response acceleration was monitored using an accelerometer attached to the middle of the board.

In addition, strain gauges were mounted at strategic locations selected on the assembly to provide data for the strains experienced by components of interest. This combination of data from acceleration sensors, the various strain gauges, and active monitoring of the resistance of the daisy-chain components provided the base data for analysis of the vibration performance of the assembly.

Sine sweep vibration was performed from 10-200 Hz at levels of 2 G and 5 G for each group, to find the resonance frequencies of the boards. Following the sweeps, each batch was subjected to sine dwell vibration for 6 h at the closest common resonance frequency causing roughly equal deflection in all test vehicles of that batch. The observed resonance frequency range of the 26 boards was 48-60 Hz. The card G level range for the first five groups, vibrated at a 5-G peak, was 45-65 G. Further investigation revealed that groups 3 and 5 had slightly higher resonance frequencies and, as a result, slightly higher card G levels. Cross-section analysis was performed on one test vehicle after the vibration test and there were no cracks found between the layers of the raw test vehicle; therefore, this resonance frequency shift for these two groups is related to material properties of these groups' boards. It was not possible to further narrow down the cause any of the shifts, due to the number of variables.

In the beginning of the sine dwell vibration, the card deflections were observed by eye to be similar, and confirmed by strain readings at strain gauge locations 1 and 12, which were at the middle of the board. These readings in the middle of the boards where maximum deflection occurs were fairly consistent across all four boards in the fixture. This suggests that the deflections are comparable. It is apparent by the collected data that the cards in group 3 bent less than all other groups, as the G level here was greater than the rest; this might suggest these test vehicles were stronger. As stated, the lesser deflection of the group 3 cards related to properties of materials of these cards due to alloy type or lamination type or surface finish.

I. Strain Monitoring

A Vishay Measurement System Strain Smart 6000 was used to measure the strain level during vibration testing. Two configurations of strain gauge attachments were used, and each included two rosettes (three axis) and six single-axis strain gauges attached to each board, for a total of 12 channels monitored. By using two configurations, we were able to maximize the use of our strain system and monitor a larger group of components and assembly locations. Two single-axis strain gauges were both vertically and horizontally centered on the front and back of the boards (locations 1 and 12 in Figs. 7-9; these locations were used as universal points, as maximum strain occurs here). Two rosette strain gauges were attached directly under the two BGA components closest to the horizontal center (locations 7-9 and 4-6), and the other four strain gauges were placed under QFPs and PLCC84s (locations 10, 11, 2, and 3).

During the sine sweep vibration for all groups, strain monitoring was performed throughout. These data were used to validate the setup and to confirm the maximum strain

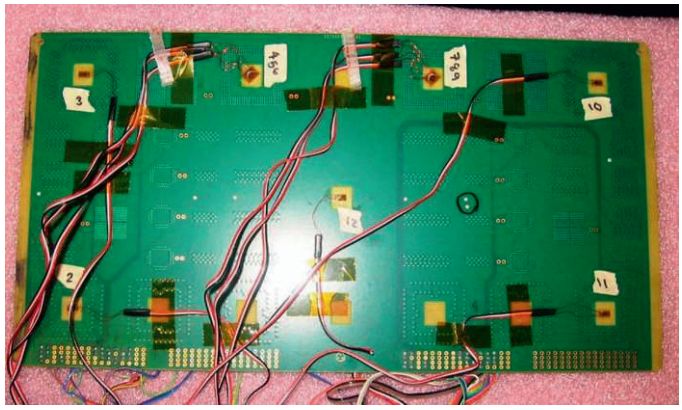

Fig. 7. Strain gauge attachment, configuration 1, bottom side.

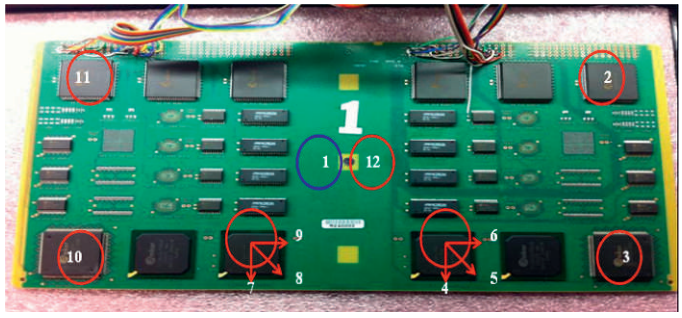

Fig. 8. Batches 1, 3, and 4. Blue indicates strain gauge on top side; red indicates strain gauge on bottom side.

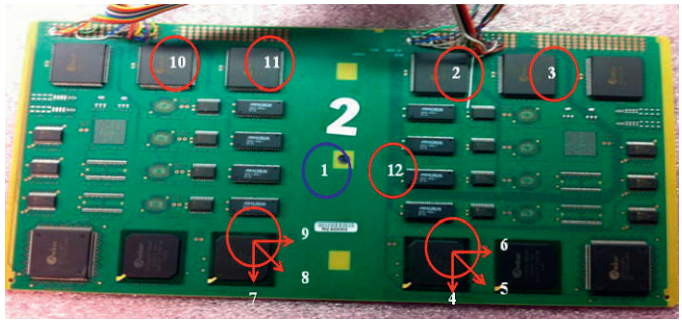

Fig. 9. Batches 2 and 5. Blue indicates strain gauge on top side; red indicates strain gauge on bottom side.

occurring at the resonance frequency. Strain monitoring only occurred for the first 5 min of each hour of the 6-h sine dwell. The scan rate was 200 data points per second. When resonance was achieved, maximum strain occurred in the center of the board, where the range was roughly 200-240 microstrain for the 5-G sweep. This suggests that the maximum deflections of all batches were very similar.

The first mode deflection was anticipated from the sine sweep and dwell testing; uniaxial strain gauges were used on most of the component locations. Rosette strain gauges were used on the BGA locations to confirm there was no other directional strain on the test sample.

J. Resistance Monitoring

All 26 test vehicles were resistance monitored during vibration testing. Sixteen components were monitored on each test vehicle. Each component was each assigned one channel in the resistance monitoring system; therefore, four test vehicles and 64 channels were monitored in each batch. The Anatech event detector data collection was set up with a cycle time of 20 s, a data collection rate of every 2 s, and the data collection duration was the full testing time. Every 2 s, the system compared the collected value to the threshold value of 300 Ω. If the measured resistance was greater than the threshold, it was considered a failure. Since cable breaks were also flagged as failures, cables were secured to the fixture with tape to provide strain relief.

Results and Discussion

In this section, the thermal effects on solder joint quality and microstructure are described first, both as assembled and after thermal cycling in ATC testing. Then, the results of mechanical testing are described, including strain analysis and resistance failures during dwells. The metallurgical analysis of mechanically stressed joints follows.

A. As-Assembled Solder Joint Quality and Microstructure

All assemblies had acceptable solder joints in terms of voiding, wetting, shape, and size. No major anomalies or concerns were noted. The maximum void percentage of the BGA352 ball is shown in Table VIII. Experimental alloys had less voiding than SAC305 and were comparable to SnPb. The lower level of voiding was found on ENEPIG, followed by ENIG, and then OSP. The typical radiographic images of voiding are shown in Fig. 10. Wetting on OSP that may be a problem with SAC305 was improved for the experimental alloys containing Bi, as shown in Fig. 11.

Table VIII
Voiding in BGA352

Assembly No.	Solder name	Surface	Voiding, %
1	Tin-Lead	OSP	15.7
2	SAC305	OSP	24.5
3	Paul	OSP	17.7
4	Violet	OSP	22.0
5	Orchid	OSP	17.2
6	SAC305	ENIG	23.2
7	Paul	ENIG	13.0
8	Violet	ENIG	12.1
9	Orchid	ENIG	12.9
10	Paul	ENEPIG	10.5
11	Violet	ENEPIG	3.5
12	Orchid	ENEPIG	10.7

Cross sections of BGA325 and QFP240 illustrating a proper solder joint shape are shown in Fig. 12. SAC305 solder balls were completely mixed with Bi-containing solders. The resulting composition was analyzed using EDX, as shown in Fig. 13. This example demonstrates a BGA325 solder joint with an SAC305 ball reflowed on an OSP board using Paul solder paste. Although the semiquantitative EDX analysis does not give a precise solder composition, it allows a comparison of solder joints formed on different surface finishes using different alloys (Table IX). The trend of reducing Ag content when the SAC 305 ball is mixed with the lower-Ag alloys, Violet and Orchid, is visible. The Cu content depends on the surface

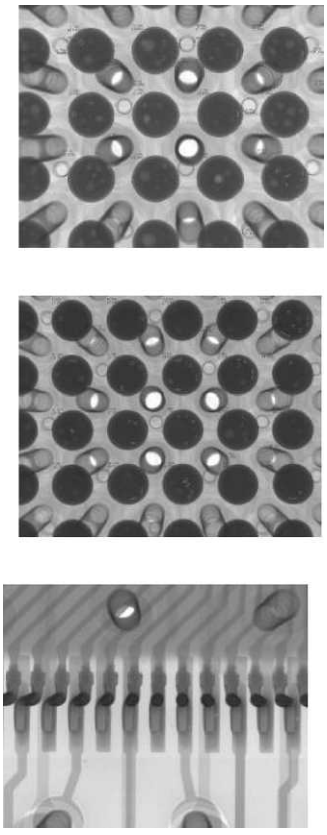

Fig. 10. Examples of voiding in experimental assemblies. (Top) BGA352, Violet on OSP. (Center) BGA352, SAC305 on OSP. (Bottom) QFP204, Paul on OSP.

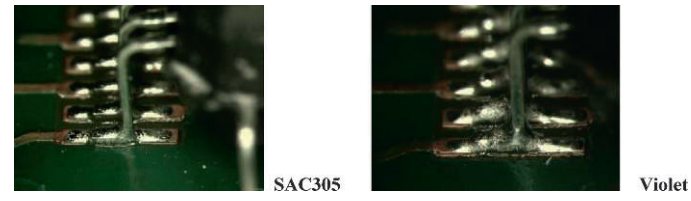

Fig. 11. Example of wetting on OSP and QFP240 (solders as labeled).

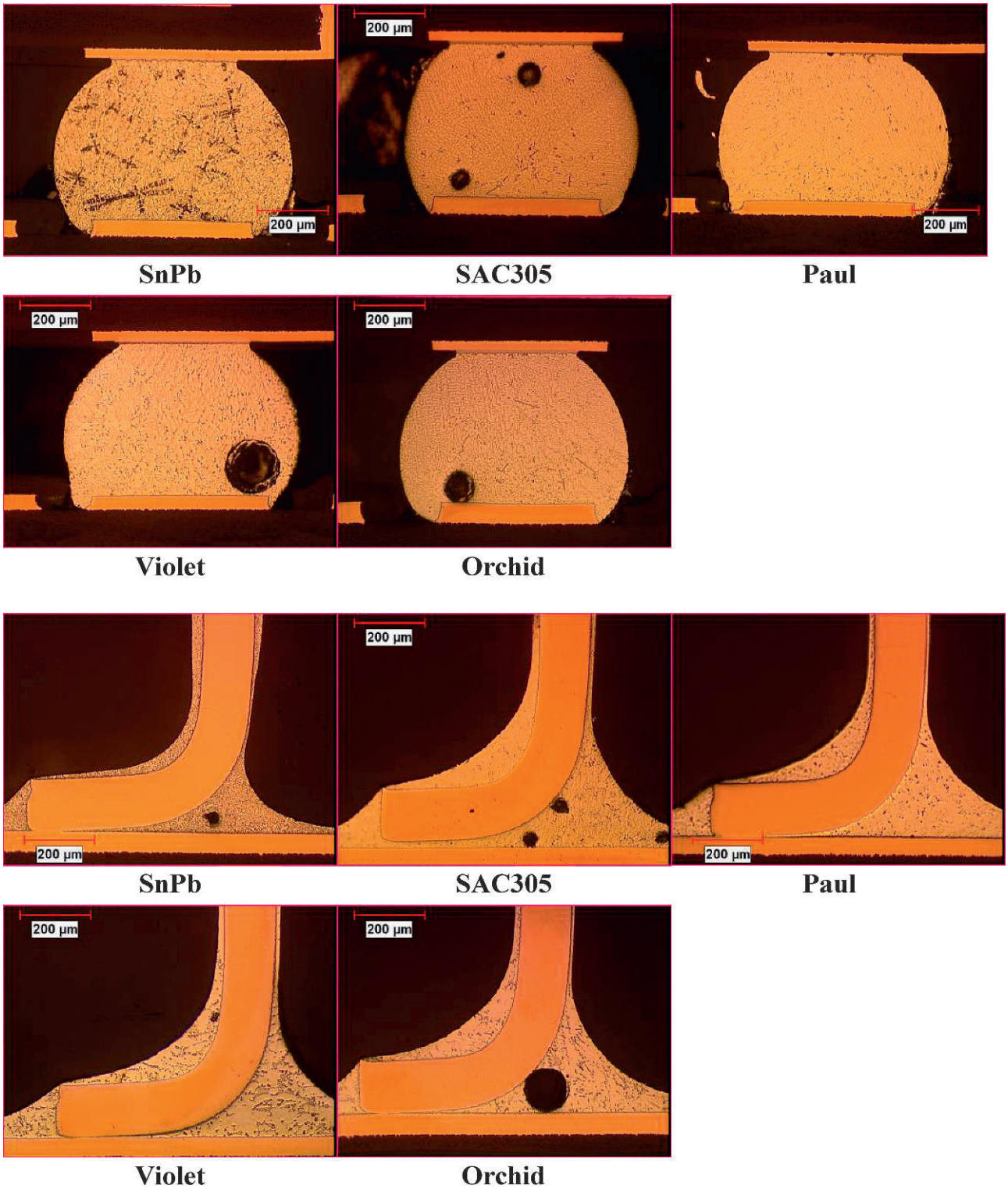

Fig. 12. BGA325 and QFP240 joint formation on OSP, ×100 magnification.

finish. The Cu is slightly lower on ENIG and ENEPIG when the joint is formed using the no-Cu alloys, Paul and Orchid. Cu dissolves in solder joints formed on OSP finished boards; even SnPb joints contain 0.4% Cu. The Cu content in Pb-free joints formed on OSP boards is about two times higher compared with the joints formed on ENIG and ENEPIG boards.

The Bi-content in BGAs was similar in all three experimental alloys and did not exceed 2.1%. The Bi content was also

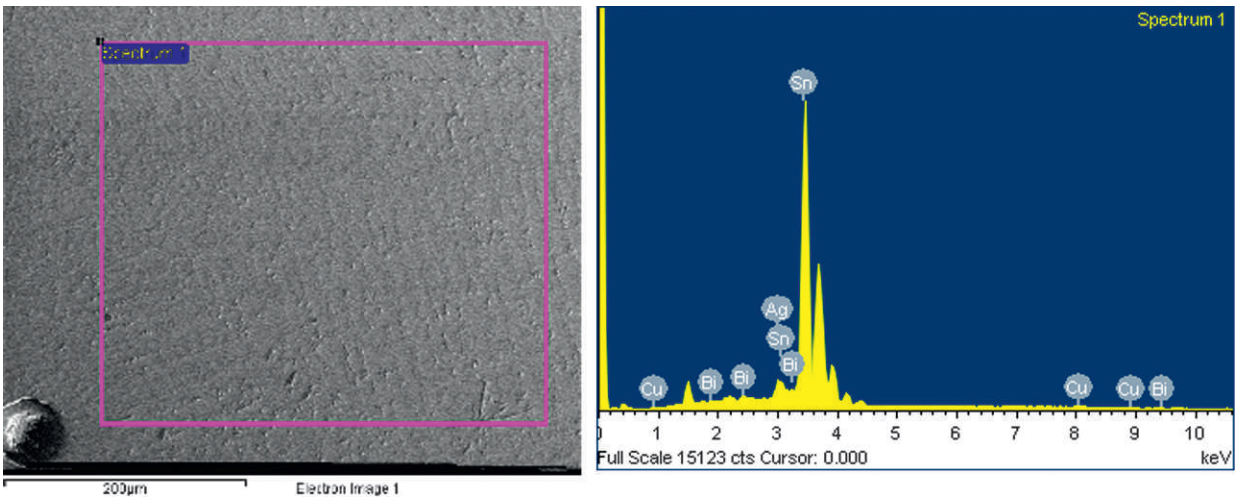

Fig. 13. EDX analysis of BGA325 formed on OSP using Paul solder paste, ×100 magnification.

Table IX
BGA352 Joint Composition

Assembly No.	Solder name	Surface finish	BGA composition				
			Sn	Ag	Cu	Bi	Pb
1	Tin-Lead	OSP	70.2	0	0.4	0	29.4
2	SAC305	OSP	96.2	2.8	1.0	0	0
3	Paul	OSP	95.0	2.6	0.8	1.7	0
4	Violet	OSP	95.7	2.1	0.7	1.5	0
5	Orchid	OSP	94.7	2.3	1.0	2.0	0
6	SAC305	ENIG	96.7	2.8	0.5	0	0
7	Paul	ENIG	95.9	3.0	0.3	0.8	0
8	Violet	ENIG	95.5	2.2	0.6	1.7	0
9	Orchid	ENIG	95.0	2.5	0.4	2.1	0
10	Paul	ENEPIG	95.0	2.5	0.4	2.1	0
11	Violet	ENEPIG	95.1	2.8	0.6	1.5	0
12	Orchid	ENEPIG	95.5	2.2	0.4	1.9	0

measured in Sn grains. The ion beam was placed in the Sn location clear of any visible precipitations. The results are shown in Fig. 13. The Bi in Sn grains is also about 2 wt% (1 atomic % [at.%]). This amount of Bi is very close to the solubility in Sn at the ambient condition (Fig. 14) and will provide solid-solution strengthening. Therefore, Bi precipitation is not expected in BGA solder joints.

The representative microstructures of the BGA352 solder joints are shown in Fig. 15. The experimental alloys have a microstructure similar to SAC305, with primary-like Sn dendrites and interdendritic eutectic: Ag_3Sn + Sn or Ag_3Sn + Cu_6Sn_5 + Sn. The diameter of Sn dendrite branches was smaller in SAC305 than in all three Bi-containing alloys. The dendritic structure in OSP joints was finer than in ENIG and ENEPIG joints. No Bi precipitation was detected in BGA352

The Sn grains in QFP240 joints contain 3-4 wt% Bi (Table X), which is about two times higher than the Bi dissolution limit at room temperature. The Bi is expected to precipitate in a Sn matrix and cause solid-solution and precipitation strengthening effects. A typical microstructure of the experimental Bi-containing alloys is shown in Fig. 15. The microstructure contains primary Sn dendrites and interdendritic

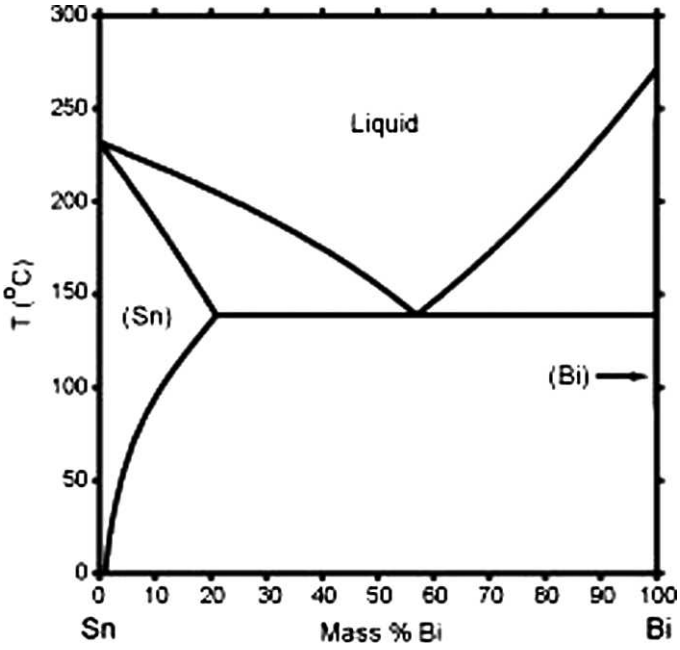

Fig. 14. Sn-Bi phase diagram showing Bi dissolution at different temperatures (source: National Institute of Standards and Technology).

eutectic: Ag_3Sn + Sn or Ag_3Sn + Cu_6Sn_5 + Sn. The Bi particles are found in the eutectic regions and inside the primary Sn grains. The dendritic structure of the QFP240 joints is also coarser in experimental alloys than in SAC305 (Fig. 16).

The intermetallic thickness was measured on both board and component sides in BGA352 and QFP240. The results are shown in Table XI. The intermetallic morphology on the board side is shown in Fig. 17 and Fig. 18. In most BGA and all QFP solder joints formed on OSP, ENIG, and ENEPIG surface finishes using SnPb, SAC305, and the three alloys containing Bi, the intermetallic does not exceed 3.9 µm. The intermetallic in Paul and Orchid BGAs on the ENEPIG board side was very thick. Because of the irregular shape, shown in Fig. 17, the thickness could not be properly measured.

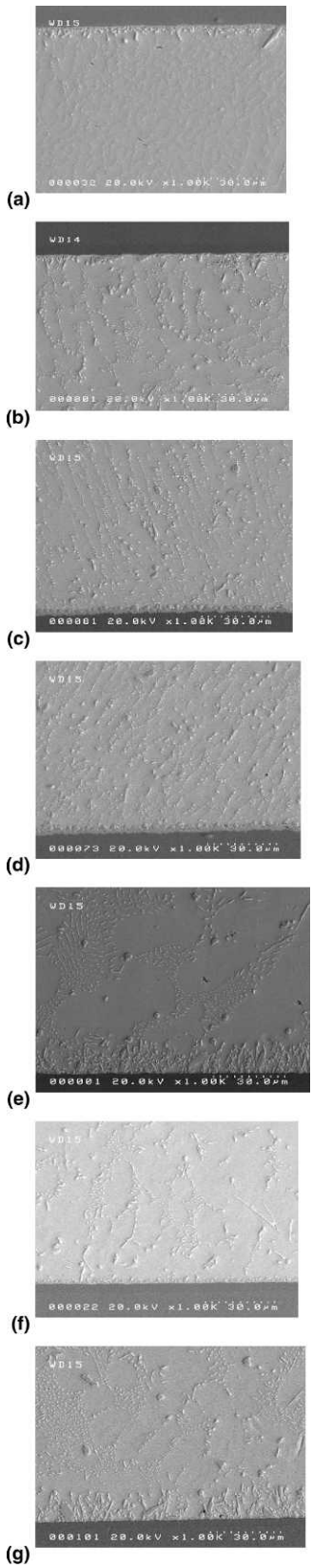

Fig. 15. Microstructure of BGA352 solder joints (scanning electron micrograph, ×1,000 magnification). (a) SAC305, OSP; (b) Paul, OSP; (c) Violet, OSP; (d) Orchid, OSP; (e) Paul, ENEPIG; (f) Violet, ENEPIG; (g) Orchid, ENEPIG.

Table X
Bi Content in Sn Grains

			QFP		BGA	
Assembly No.	Solder name	Surface finish	Wt %	At.%	Wt %	At.%
1	Tin-Lead	OSP	0	0	0	0
2	SAC305	OSP	0	0	0	0
3	Paul	OSP	3.1	1.8	1.5	0.9
4	Violet	OSP	3.8	2.2	1.4	0.8
5	Orchid	OSP	3.8	2.2	2.1	1.2
6	SAC305	ENIG	0	0	0	0
7	Paul	ENIG	3.8	2.2	1.2	0.7
8	Violet	ENIG	3.7	2.1	1.9	1.1
9	Orchid	ENIG	4.1	2.4	2.4	1.4
10	Paul	ENEPIG	4.0	2.3	2.0	1.1
11	Violet	ENEPIG	3.5	2.0	2.0	1.1
12	Orchid	ENEPIG	3.5	2.0	1.6	0.9

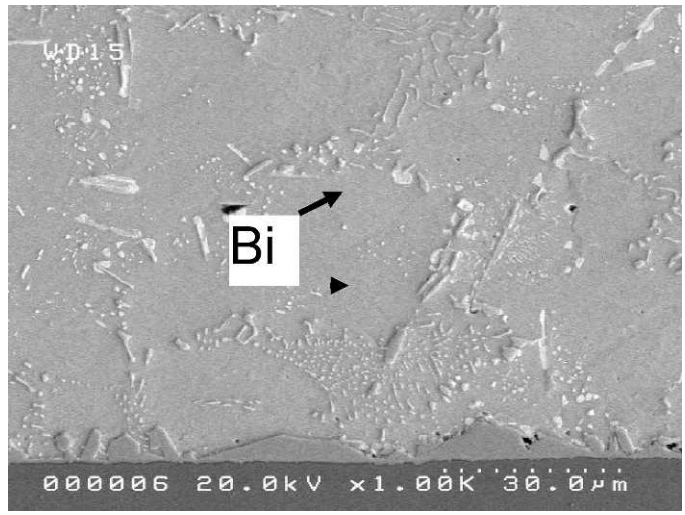

Fig. 16. Microstructure of QFP240 solder joints, Paul, ENEPIG (scanning electron micrograph, ×1,000 magnification).

Excluding Paul and Orchid on ENEPIG, the thickest intermetallic in BGAs grew in SAC305 joints on OSP surface finish. This thickness is attributed to the higher reflow process temperature. In QFPs, the thickest intermetallic was formed in the Orchid alloy. This alloy had the widest pasty range and remained in the liquid stage for a longer time during reflow. The intermetallic in Paul was in a thicker range compared with Violet. The intermetallic in Violet was always thinner and properly formed, and of the same thickness on all surface finishes. Only the Violet intermetallic layer had a regular proper shape on the ENEPIG finish, as shown in Fig. 17 and Fig. 18.

Solder joint properties depend on the intermetallic type and the morphology of the interfacial layer, in addition to joint thickness. The morphology is deeply dependent on the intermetallic lattice and composition. The EDX analyses were performed on the board and component sides of both BGA352 and QFP240. The type and the composition of the interfacial intermetallic layers are shown in Table XII. SnPb and Pb-free

Table XI
Intermetallic Thickness

Assembly No.	Solder name	Surface finish	QFP, IMC thickness, µm		BGA, IMC thickness, µm	
			Board	Component	Board	Component
1	Tin-Lead	OSP	1.8	2.0	2.2	2.1
2	SAC305	OSP	2.1	2.5	3.3	2.4
3	Paul	OSP	1.9	1.9	2.4	1.5
4	Violet	OSP	1.9	2.2	2.1	1.7
5	Orchid	OSP	2.0	2.2	2.4	1.6
6	SAC305	ENIG	1.2	2.3	1.6	1.4
7	Paul	ENIG	2.1	3.6	1.0	1.3
8	Violet	ENIG	1.7	2.6	2.1	1.2
9	Orchid	ENIG	2.9	3.5	1.9	1.5
10	Paul	ENEPIG	1.5	3.5	Irregular	1.7
11	Violet	ENEPIG	1.8	2.1	1.1	0.9
12	Orchid	ENEPIG	3.9	3.2	Irregular	1.6

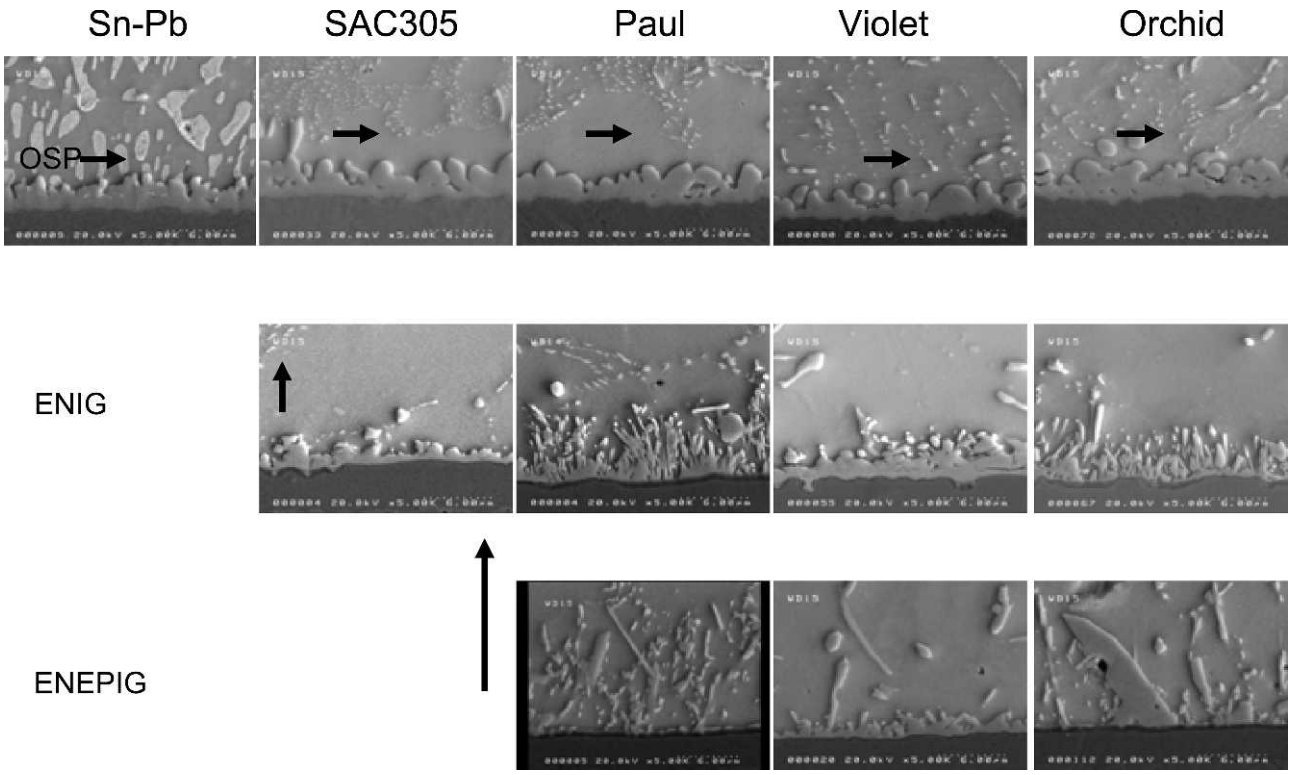

Fig. 17. Intermetallic formation in BGA352 (scanning electron micrograph, ×5,000 magnification). OSP: Arrows show the compact IMC. A less uniform IMC forms on ENIG, and the IMC on ENEPIG is nonuniform.

solders—SAC305 and three Bi-containing alloys—form Cu_6Sn_5 compound on OSP finished boards. The OSP protective coating rapidly dissolves in liquid solder, and then Cu dissolves in liquid tin and forms Cu_6Sn_5. Cu_6Sn_5 (η-phase) has a hexagonal close-packed structure. In the BGAs, up to 4%Ni substitutes the Cu in the intermetallic (Fig. 19). The interfacial intermetallic layers have a nodule morphology typical for Cu_6Sn_5, as shown in Figs. 17-19.

The intermetallic reaction layer formed between Ni/Au-finished component pads and the SAC305 solder ball contained about 20-25 at.%Ni, 30-35 at.% Cu, and 42-45 at.% Sn, and was found to be a ternary compound. The existence of this compound in a SnNiCu system was shown by Obemdorff in 2001 [13] and was confirmed by L. Snugovsky et al. [14] in 2005. As shown in [13], this ternary compound corresponds to the formula $Ni_{23}Cu_{33}Sn_{44}$. This type of intermetallic forms on ENIG and ENEPIG finished boards when soldered using SAC305 or Violet. Both solders contain 0.5% Cu. The interfacial intermetallic layer has a rather smooth cellular morphology.

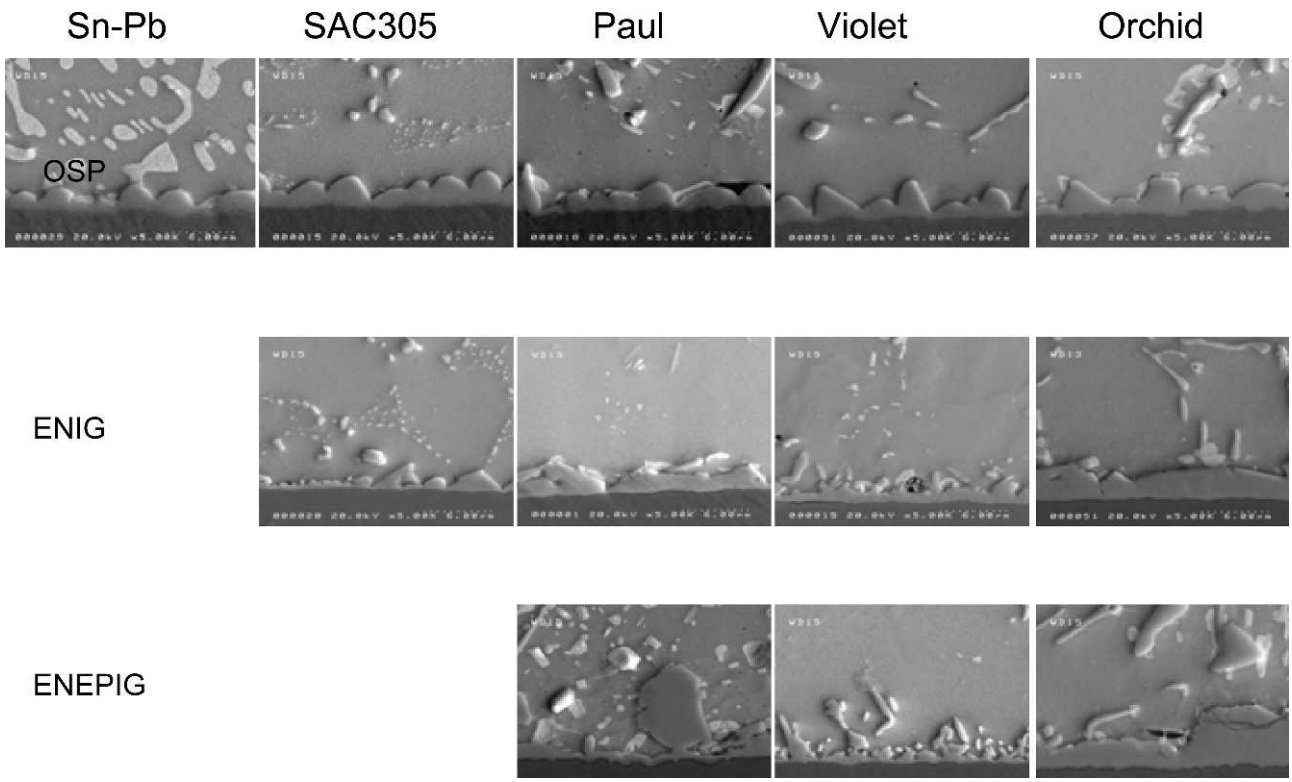

Fig. 18. Intermetallic formation in QFP240 (scanning electron micrograph, ×5,000 magnification).

Table XII
Intermetallic Type

Assembly No.	Solder name	Surface finish	QFP IMC type		BGA IMC type	
			Board	Component	Board	Component
1	Tin-Lead	OSP	Cu_6Sn_5	Cu_6Sn_5	$(Cu,Ni)_6Sn_5$	$Cu_{23}Ni_{33}Sn_{44}$
2	SAC305	OSP	Cu_6Sn_5	Cu_6Sn_5	$(Cu,Ni)_6Sn_5$	$Cu_{23}Ni_{33}Sn_{44}$
3	Paul	OSP	Cu_6Sn_5	Cu_6Sn_5	$(Cu,Ni)_6Sn_5$	$Cu_{23}Ni_{33}Sn_{44}$
4	Violet	OSP	Cu_6Sn_5	Cu_6Sn_5	$(Cu,Ni)_6Sn_5$	$Cu_{23}Ni_{33}Sn_{44}$
5	Orchid	OSP	Cu_6Sn_5	Cu_6Sn_5	$(Cu,Ni)_6Sn_5$	$Cu_{23}Ni_{33}Sn_{44}$
6	SAC305	ENIG	$(Cu,Ni)_6Sn_5$	$(Cu,Ni)_6Sn_5$	$Cu_{23}Ni_{33}Sn_{44}$	$Cu_{23}Ni_{33}Sn_{44}$
7	Paul	ENIG	$Cu_{23}Ni_{33}Sn_{44}$	$(Cu,Ni)_6Sn_5$	$(Ni,Cu)_3Sn_4$	$Cu_{23}Ni_{33}Sn_{44}$
8	Violet	ENIG	$Cu_{23}Ni_{33}Sn_{44}$	$(Cu,Ni)_6Sn_5$	$Cu_{23}Ni_{33}Sn_{44}$	$Cu_{23}Ni_{33}Sn_{44}$
9	Orchid	ENIG	$Cu_{23}Ni_{33}Sn_{44}$	$(Cu,Ni)_6Sn_5$	$(Ni,Cu)_3Sn_4$	$Cu_{23}Ni_{33}Sn_{44}$
10	Paul	ENEPIG	$(Cu,Ni,Pd)_6Sn_5$	$(Cu,Ni,Pd)_6Sn_5$	$(Ni,Cu)_3Sn_4 + (Pd,Au,Ni,Cu)Sn_4$	$Cu_{23}Ni_{33}Sn_{44}$
11	Violet	ENEPIG	$(Cu,Ni,Pd)_6Sn_5$	$(Cu,Ni,Pd)_6Sn_5$	$Cu_{23}Ni_{33}Sn_{44}$	$Cu_{23}Ni_{33}Sn_{44}$
12	Orchid	ENEPIG	$(Cu,Ni,Pd)_6Sn_5$	$Cu_{23}Ni_{33}\ Sn_{44} + (Cu,Ni,Pd)_6Sn_5$	$Cu_{23}Ni_{33}Sn_{44} + (Ni,Cu)_3Sn_4 + (Pd,Au,Ni,Cu)Sn_4$	$Cu_{23}Ni_{33}Sn_{44}$

In BGAs assembled on ENIG boards, Paul and Orchid alloys that do not have Cu in their composition form the Ni-based $(Ni,Cu)_3Sn_4$ compound. This compound is typical for Cu content lower than 0.2% [15]. The solders with lower melting temperature started forming intermetallic immediately after melting, before a SAC305 solder ball fully dissolved in liquid. The Cu introduced during mixing substituted Ni up to 4 at.%. The $(Ni,Cu)_3Sn_4$ intermetallic layer had a sharp needle-like structure (Fig. 17).

In BGAs assembled on ENEPIG boards using Paul and Orchid alloys, Pd-containing intermetallic formed, in addition to the $(Ni,Cu)_3Sn_4$ compound (Fig. 20). This intermetallic also contained some Au, Ni, and Cu atoms in a composition close to the $MeSn_4$ formula. The reaction intermetallic layers between ENEPIG and both no-Cu, ternary SnAgBi alloys, Paul and Orchid, were extremely nonuniform, irregular in shape, and had needle–like morphology (Fig. 17 and Fig. 20a).

In QFPs assembled on ENEPIG boards, Pd was dissolved in the board and component side $(Cu,Ni,Pd)_6Sn_5$ compounds (Fig. 20b). Pd-based needles were found in the bulk solder of all solder joints formed on the ENEPIG finished boards (Fig. 20c).

The proper formation of interfacial intermetallic layers in solder joints is important for harsh-environment applications. The intermetallic forms a metallurgical bond to common basis materials and, if it is a solid thin layer, it has a strengthening

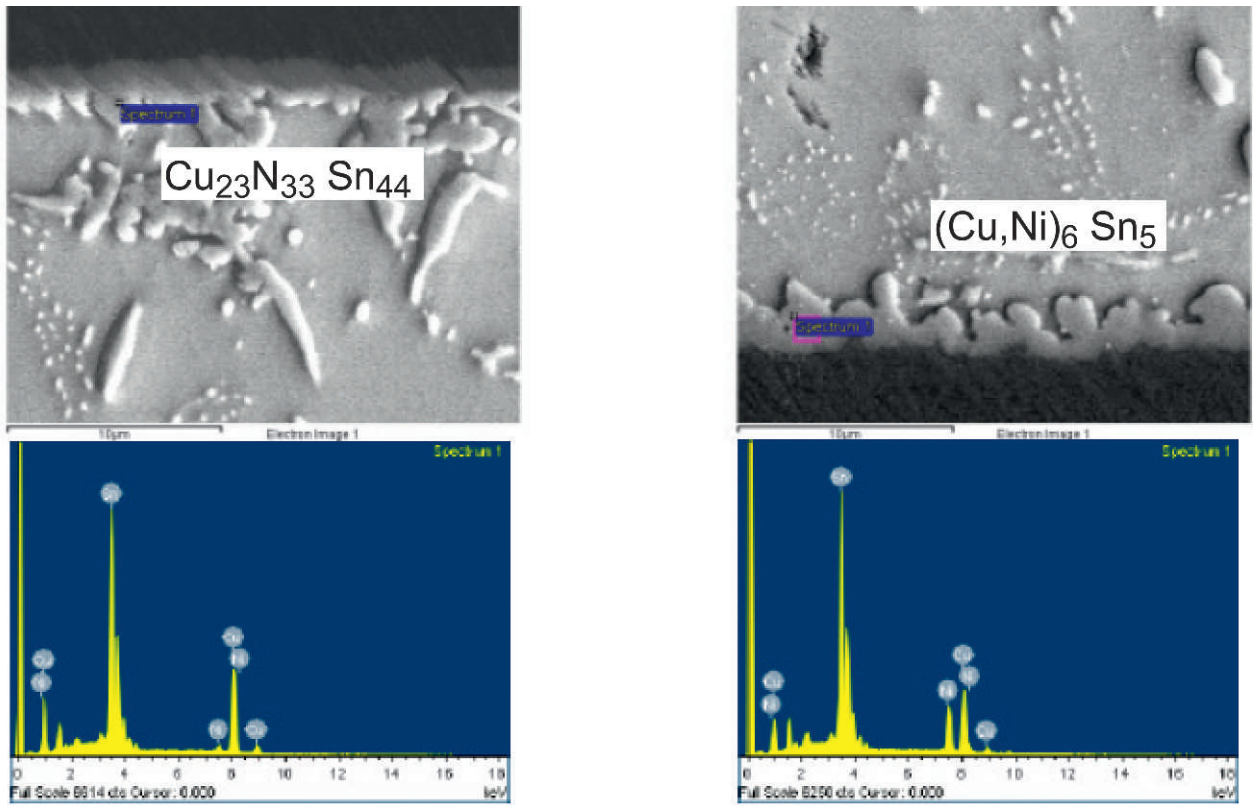

Element	Weight%	Atomic%
Ni K	1.7	2.7
Cu K	36.6	51.2
Sn L	61.7	46.2
Totals	100.0	

Element	Weight%	Atomic%
Ni K	13.6	20.1
Cu K	25.8	35.4
Sn L	60.6	44.5
Totals	100.0	

(a) (b)

Fig. 19. EDX analysis of BGA352 solder joint, Paul, OSP. (a) board side; (b) component side.

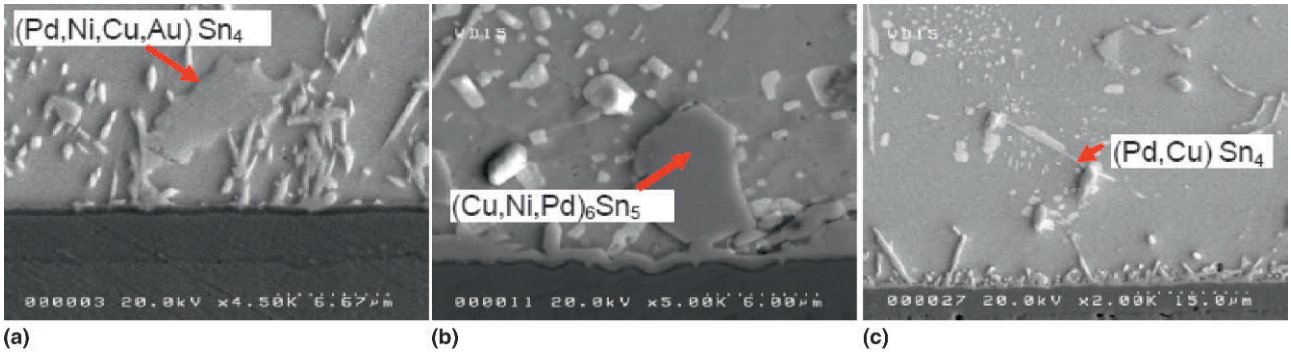

(a) (b) (c)

Fig. 20. Pd-containing intermetallics in solder joint, ENEPIG. (a) BGA352, Paul; (b) QFP240, Orchid; (c) BGA352, Violet.

effect on solder joints. However, if the interfacial intermetallic layers are thick, they can cause joint embrittlement. A needle-like, irregular, intermetallic morphology causing stress concentration may reduce the reliability of solder joints. The solder interconnections perform differently under thermal cycling and drop-test conditions. The reliability of electronic products relating to the mechanical properties of intermetallic reaction layers is especially important for harsh environments, where

the products experience mechanical shock loadings. As the strain rate increases, the stresses in solder interconnections also increase. The intermetallic compound layers will experience significantly higher stresses than those in thermal cycling. Hence, the properties of intermetallic layers, but not those of solder, mainly determine the fracture behavior of the interconnections under high strain rates [16]. The fracture toughness of the joints decreases rapidly with increases in the intermetallic reaction layer thickness. Therefore, the interfacial intermetallic thickness and morphology should be carefully considered in solder alloy selection.

B. ATC Reliability Test Results and Analysis

A total of 3,010 cycles of ATC were completed. There were no solder joint failures on either high or normal T_g boards after 1,548 cycles at temperatures ranging from −55°C to 125°C [17]. However, there were via failures in normal T_g boards with OSP finish, assembled using SAC305, Sn3.4Ag4.8Bi (Paul), and SnPb solders. Of these via failures on normal T_g OSP finished boards, only the SAC305 cell did not meet the aerospace qualification requirement of 1,000 cycles. Boards assembled using Violet and Orchid did not fail.

The failures isolated to the component location on the 155°C T_g boards are shown in Table XIII. These 18 failures were subjected to careful failure analysis. The failed components were cut off the boards and locations of failure were electrically determined. Cross sections were done through the solder joint and through the related via. The cross sections of the solder joints and vias are shown in Fig. 21 and Fig. 22, respectively. The solder joints are absolutely robust. Not even microcracks were found in SSOP48, QFP240, and PLCC84. A tiny microcrack was detected in one of the Paul BGA352 solder joints at the component side. Slightly longer cracks propagated through solder close the component side in the SnPb BGA352. The failures were caused by via failures. The cracks were circular and responsible for open circuits. In the ENIG and ENEPIG cells, via cracks were arrested by the Ni barrier layer and did not cause an electrical failure. Early failure of vias in SAC305 cells is attributed to the higher process temperatures that stress the normal T_g board material. The role of the new solder alloy composition in these failures is not fully understood yet. The lack of cracks in vias in cells with the lower Ag-content alloys Violet and Orchid might be attributed to their higher compliances and stress absorption in the component locations.

Table XIII
Failure Isolated to Component Locations and Confirmed Via Failures in 155°C T_g OSP Assemblies

Component type	Cycles to failure, −55°C to 125°C	Solder paste
SSOP48	853	SAC305
SSOP48	1,072	Paul
SSOP48	1,255	Paul
SSOP48	1,290	Paul
SSOP48	1,256	SnPb
SSOP48	1,287	SnPb
QFP240	485	SAC305
QFP240	1,062	Paul
QFP240	1,275	Paul
QFP240	1,287	Paul
PLCC84	1,005	Paul
PLCC84	1,464	Paul
PLCC84	1,504	Paul
BGA352	504	SAC305
BGA352	598	SAC305
BGA352	1,043	Paul
BGA352	1,067	Paul
BGA352	1,341	SnPb

Between 1,548 and 3,010 cycles, only three failures were recorded. These included one BGA built using SnPb solder and SnPb solder balls (1,734 cycles) and two BGAs built using Violet solder paste and SAC305 solder balls (2,076 cycles and 2,466 cycles), all on an OSP finish. Cross-sectioning revealed board failure due to barrel cracks through the via, as seen in Fig. 23. Almost-complete cracks were found in the SnPb BGA solder joint (SnPb on OSP) (Fig. 24). Only partial cracks were formed in the Violet BGA (Fig. 25); the electrical failures in this case were attributable to barrel cracks found within the board materials, specifically cracking of the vias.

Further examination of the microstructural changes that occurred during ATC can best be done on the QFPs, where the solder joint composition is that of the solder paste, as opposed to the BGAs, where the solder joint is a combination of the solder paste and the SAC305 solder ball. While no electrical failures were recorded on QFPs with any of the solders tested, cross sections were prepared for this analysis.

Fig. 26 and Fig. 27 show the microstructure changes that were observed in the SnPb alloy solder joints. A significant degree of recrystallization and grain growth occurs during the ATC process, resulting in much larger grains and a much larger intermetallic compound (IMC) attach layer. Crack propagation was observed between the grains, and between the phases as well as along the IMC layer in the case of eutectic SnPb. Fig. 27 also shows significant pooling of the Pb phase at the IMC layer. This phase may provide a location for crack propagation.

From Fig. 28 and Fig. 29, one can see the transformation of the SAC305 solder joint between the initial condition and after 3,010 cycles. The grains at time zero appear to be surrounded by Ag_3Sn particles and appear significantly smaller than the grains visible after ATC. Also after ATC, the Ag_3Sn particles appear to have coalesced into fewer, larger particles. Additionally, the IMC layers formed between the lead and solder, as well as between the solder and copper pad, have increased in size and appear to have two phases, Cu_3Sn and Cu_6Sn_5, as seen in Fig. 29. A Cu_3Sn layer did not appear to be significant at time zero.

The Bi-containing alloy called Paul seen in Fig. 30 and Fig. 31, with approximately 4.8% Bi, showed grain coarsening and IMC growth similar to that seen in SAC305, although the grain growth did not appear to be as dramatic as seen in SAC305.

The other Bi-containing alloys, Violet and Orchid, contained 6% and 7% Bi, respectively. This amount of bismuth appears to have impacted the microstructure in a significantly different manner during ATC. While the IMC layer grew in a similar fashion to the other alloys, the grains do not appear to have coarsened, as seen in Fig. 32 and Fig. 33. Additionally, the Bi which had previously been present largely in solid solution with Sn (Fig. 34 and Fig. 35), appears to have been largely precipitated out of the solid solution. This Bi appears to be randomly

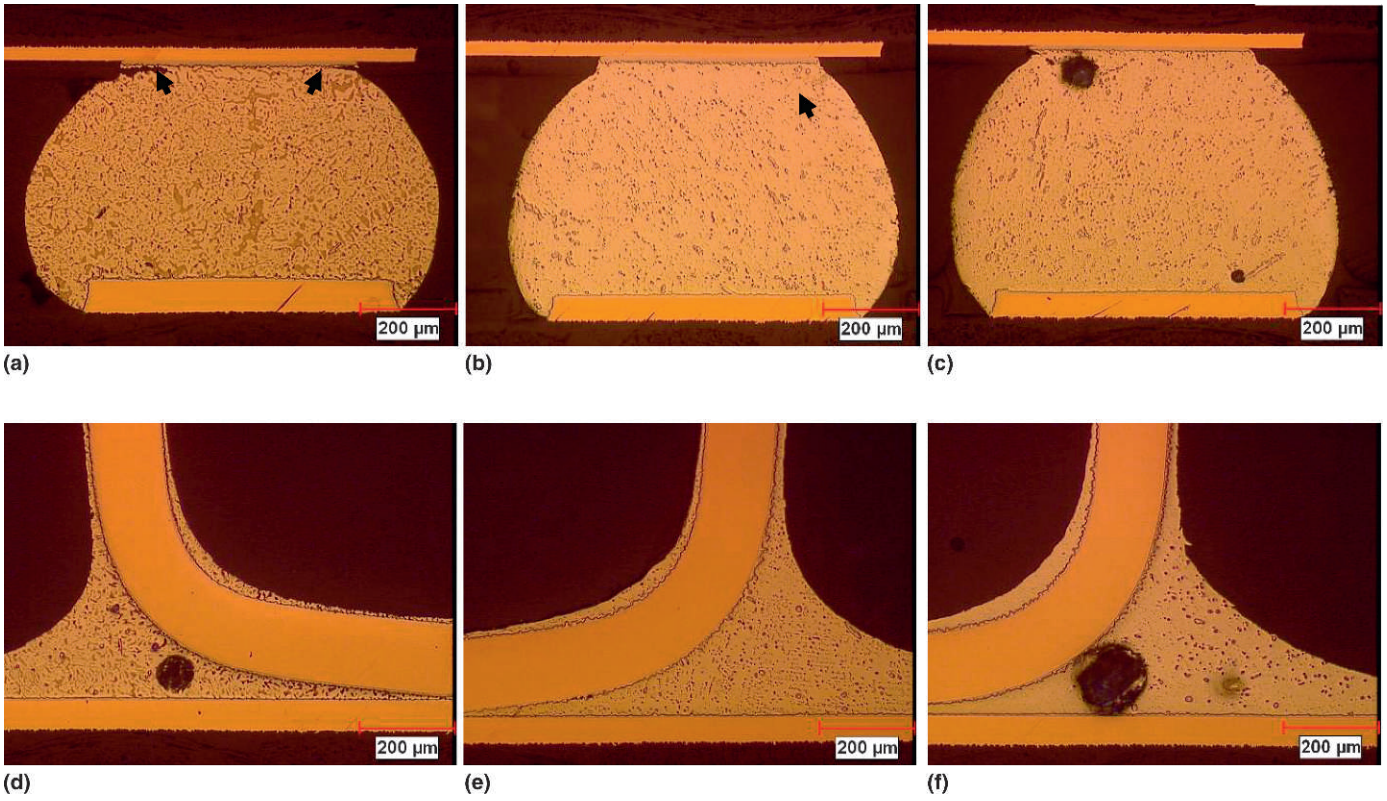

Fig. 21. Microstructure of solder joints formed on 155°C T_g boards with OSP finish after −55°C to 125°C cycling. (a) BGA352, SnPb, 1,341 cycles; (b) BGA352, Paul, 1,067 cycles; (c) BGA352, Paul, 1,043 cycles; (d) SSOP48, SnPb, 1,256 cycles; (e) SSOP48, Paul, 1,255 cycles; (f) SSOP48, SAC305, 853 cycles.

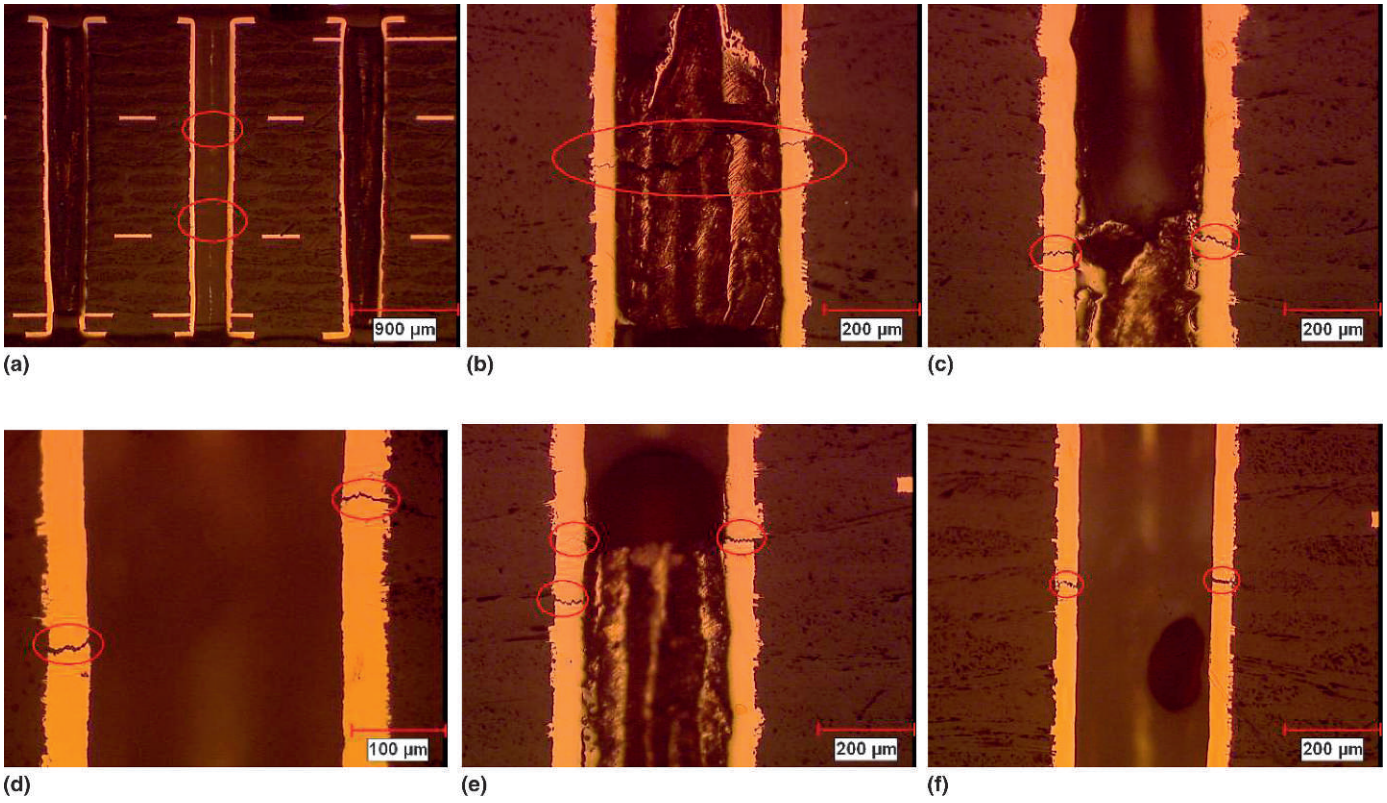

Fig. 22. Broken vias on 155°C T_g boards with OSP finish after −55°C to 125°C cycling. (a) Typical location; (b) circular shape; (c) BGA352, Paul, 1,067 cycles; (d) BGA352, Paul, 1,067 cycles, another via location; (e) SSOP48, SAC305, 853 cycles; (f) SSOP48, SnPb, 1,256 cycles.

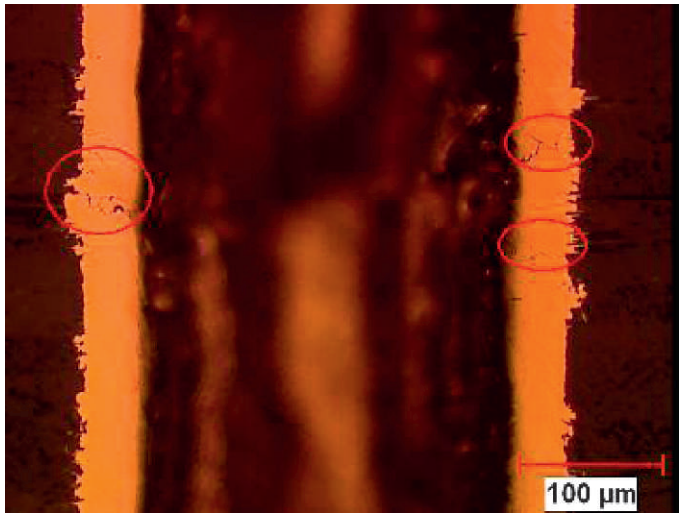

Fig. 23. Via beneath BGA SnPb on OSP.

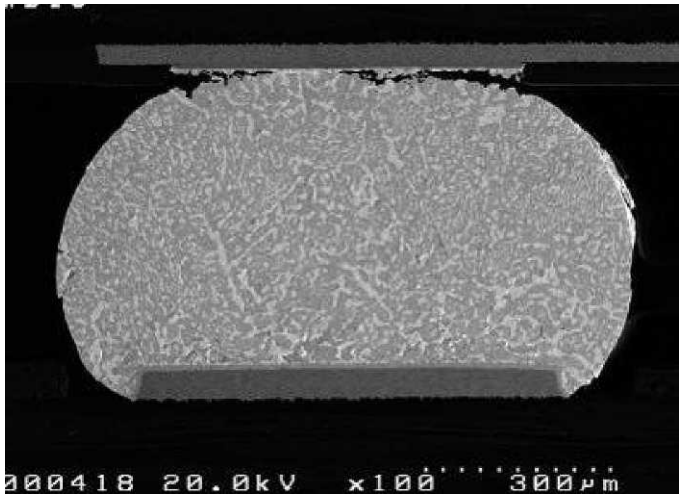

Fig. 24. SnPb on OSP.

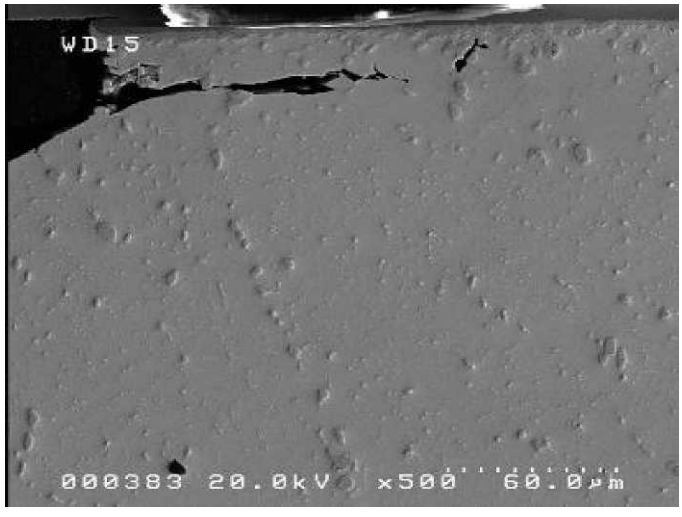

Fig. 25. Violet on OSP.

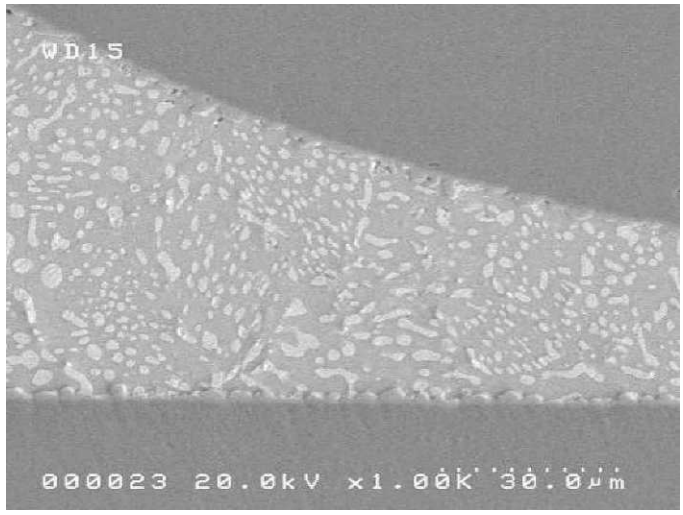

Fig. 26. SnPb at Time 0.

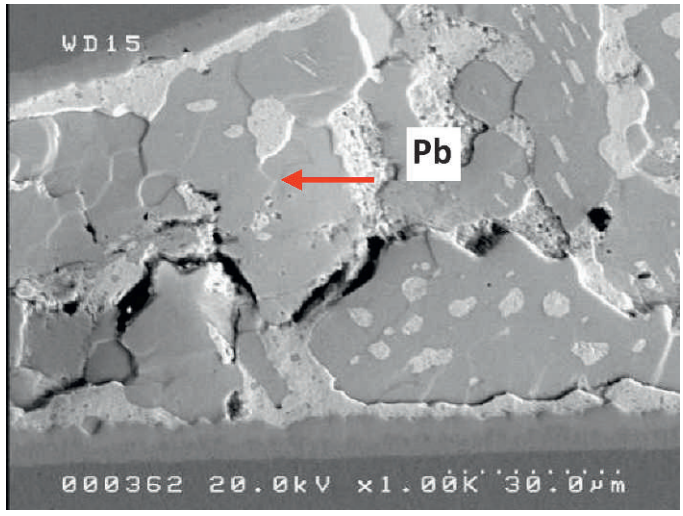

Fig. 27. SnPb after ATC.

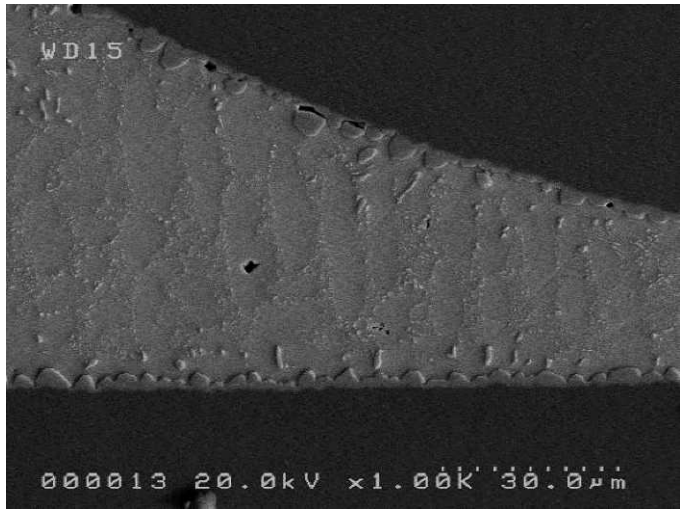

Fig. 28. SAC305 at Time 0.

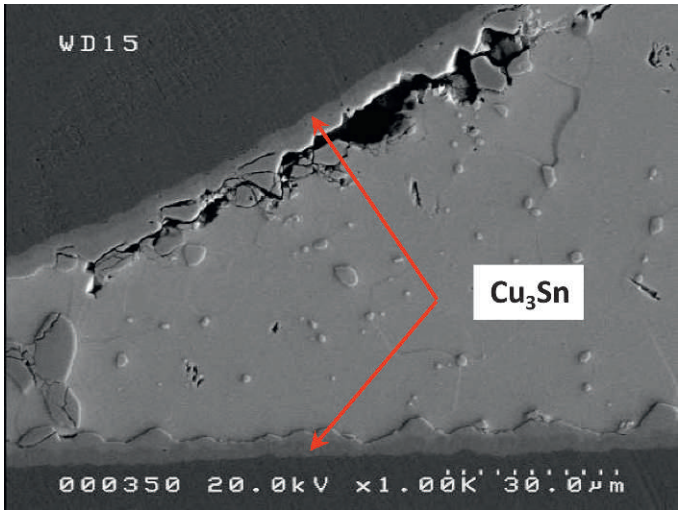

Fig. 29. SAC305 after ATC.

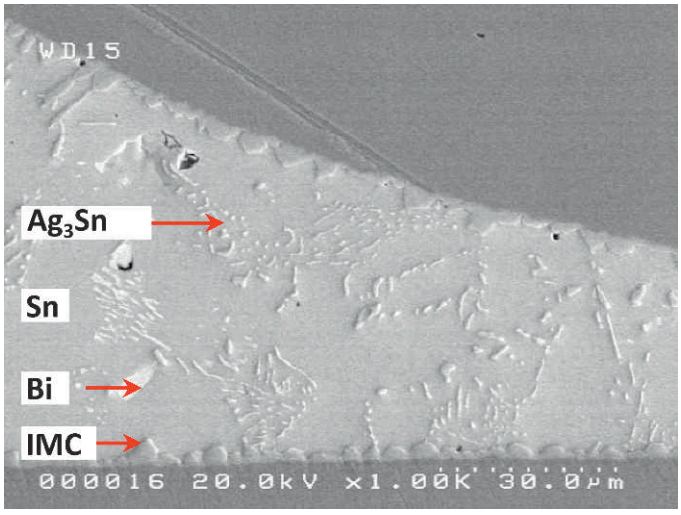

Fig. 30. Paul at Time 0.

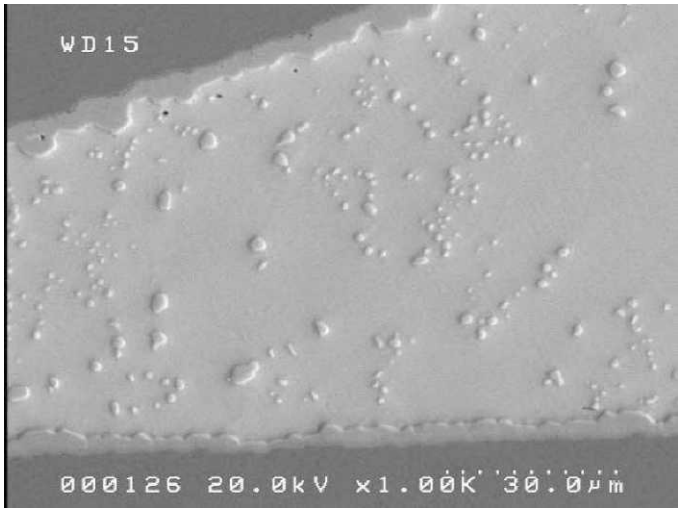

Fig. 31. Paul after ATC.

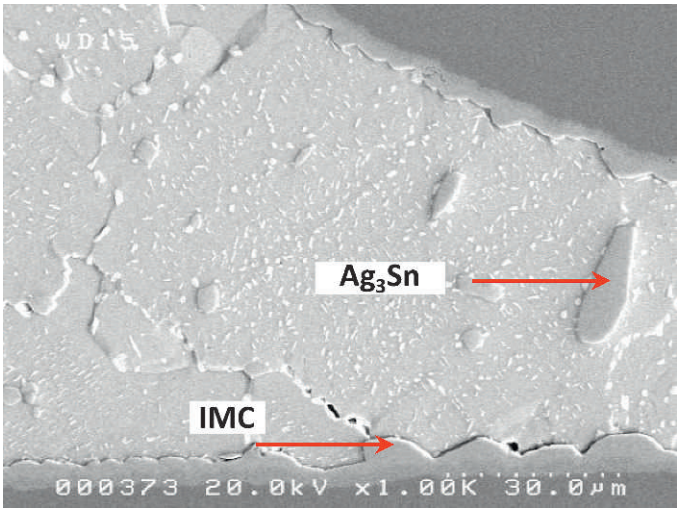

Fig. 32. Violet after ATC.

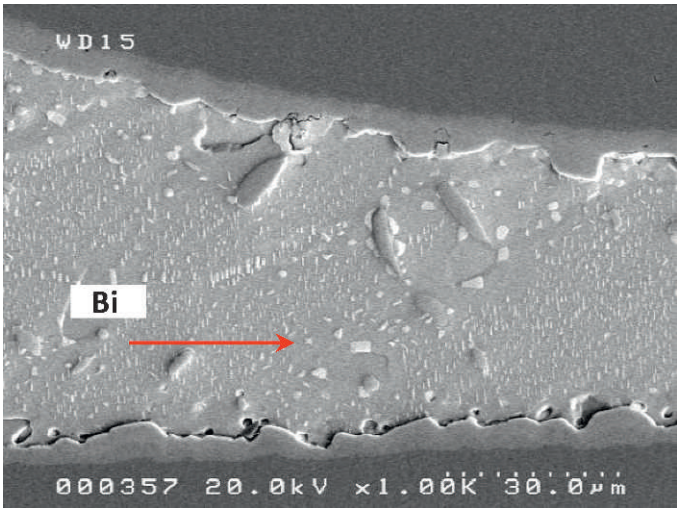

Fig. 33. Orchid after ATC.

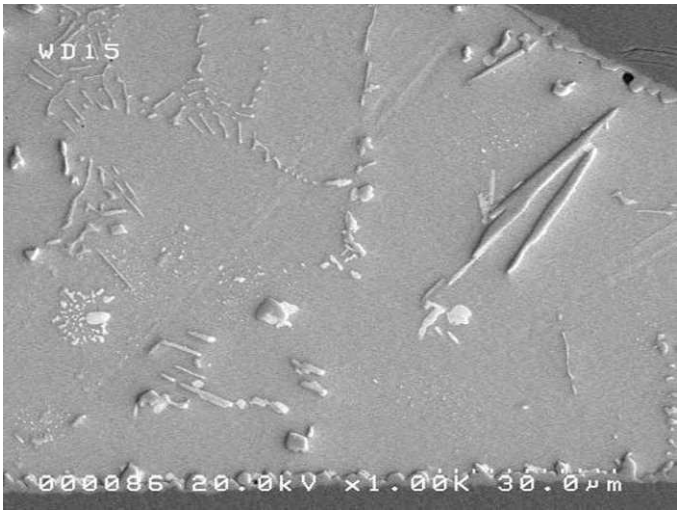

Fig. 34. Violet at Time 0.

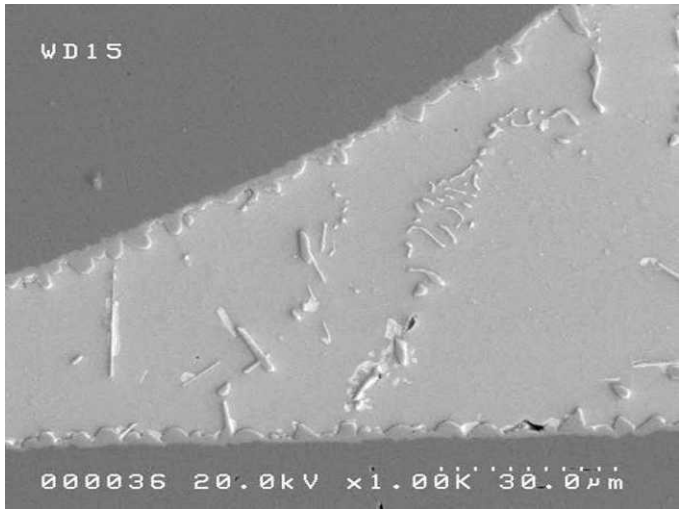

Fig. 35. Orchid at Time 0.

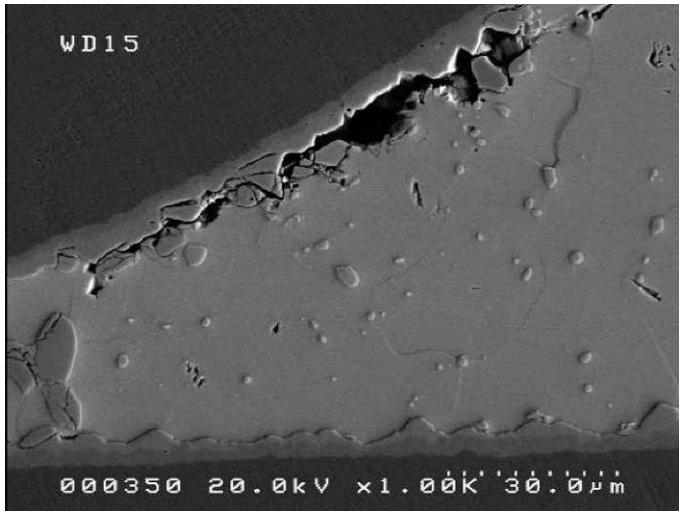

Fig. 36. SAC305 after ATC (QFP crack formation).

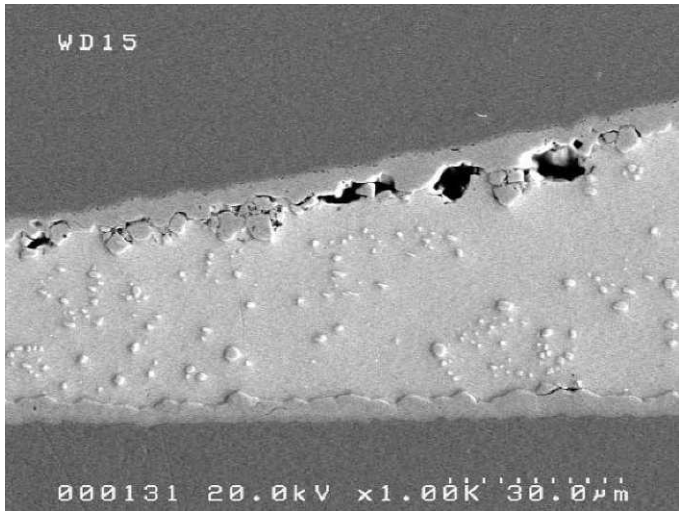

Fig. 37. Paul after ATC (QFP crack formation).

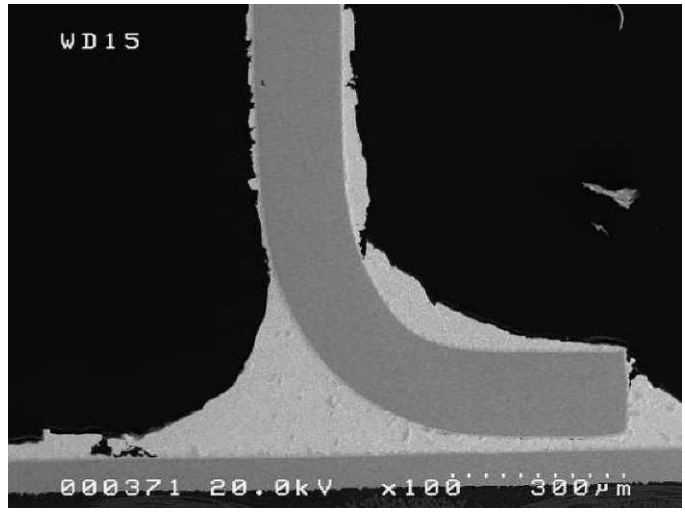

Fig. 38. Violet after ATC (no major crack).

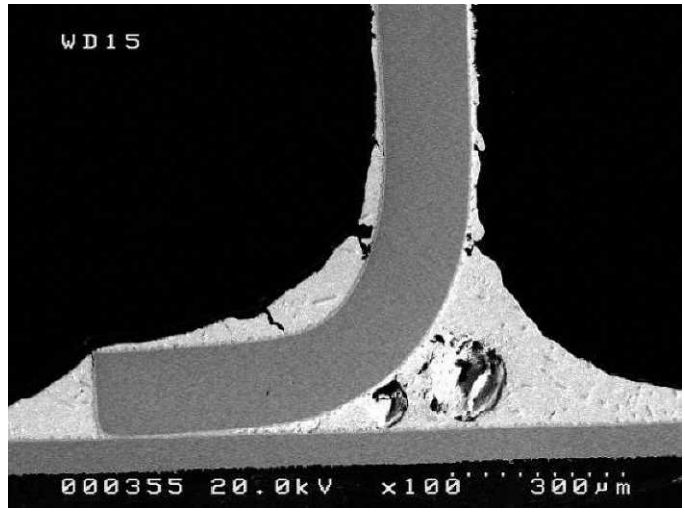

Fig. 39. Orchid after ATC (no major crack).

distributed throughout the solder joint and has not settled preferentially at the IMC layer in the same manner as Pb does in the SnPb alloy. In the scanning electron microscope images, it appears as very small white particles in the grey Sn matrix.

In SAC305 and Paul solder joints, cracks began to propagate primarily along the lead-side IMC, as seen in Fig. 36 and Fig. 37, although none was significant enough to lead to an electrical failure. This type of crack propagation was not seen in the alloys with higher Bi content, Violet and Orchid, as shown in Fig. 38 and Fig. 39.

C. Vibration Testing Using 2- and 5-G Harmonic Dwells

Sine sweeps revealed that for all these samples, the first mode average resonance frequency was 52 Hz. The response accelerometer, which was attached on the geometrical center of the board, had an average G level at resonance of 55 G at an input G level of 5 G. Therefore, the average transmissibility, the ratio between input and output, was 10.5. The sine sweep

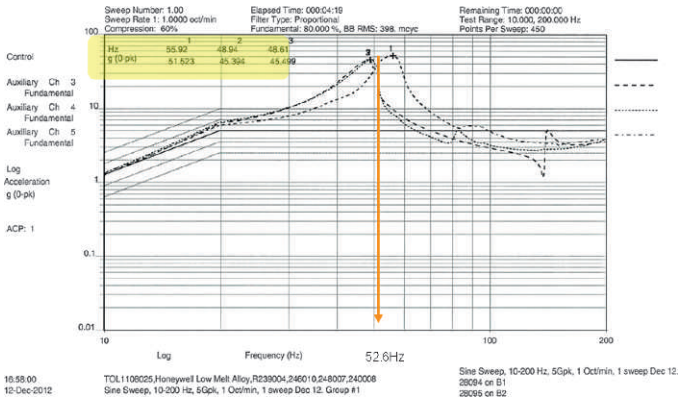

Fig. 40. Typical 5-G sweep. Resonance frequency, 52.6 Hz. This is the frequency at which individual card response plots intersect and cause almost an equal amount of deflection on all cards.

graph in Fig. 40 illustrates the test vehicles' response acceleration at their resonance frequencies. The resonance amplitude in displacement was 0.4 inches peak to peak, and due to this high displacement, the board experienced a large bending momentum, which led to component solder failure. For the 5-G and 2-G sweeps, the average test vehicle G levels at resonance frequencies were 54.78 G and 35.48 G, respectively. Test vehicle response G levels were measured only at the beginning. The G level deviations during the dwell were not measured. The frequency was held constant throughout the test. The groups 6, 7, and 8 were assigned to the 2-G dwell, and the decision was made not to attach the strain gauges, since we did not expect many failures from the 2-G dwell. The test results are shown in Table XIV.

As expected, more failures happened during the first 2 h of sine dwell testing at the 5-G peak, and this failure pattern was noted on all 5-G testing. Specifically, the BGAs, populated closer to the center of the test samples and experiencing high deflection, failed within the first 2 h of dwell testing. The strain level distribution on the test samples was high at the beginning of the dwell and there was a significant drop in strain levels after about 2 h of testing. The noted drop in strain level validated the early stage BGA failures.

In Table XIV, the maximum strains on the component side of the test vehicle measured with strain gauge 1 compared with the maximum strains measured on the opposite side with strain gauge 12 are consistently lower, due in part to the slight shift of the neutral axis toward the component side. Theoretically, the compressive strains should be close to the tensile strains and are close for strain gauge 1, but in the strain gauge 12 measurements, only batches 4 and 5 are close. The strain gauge numbering corresponds to the channel numbering shown in Table XV.

D. Strain Testing

The strain raw data for each testing batch were extracted from the strain system and processed in Microsoft Excel. Then the strain versus time graphs were created for each strain gauge location. The strain graphs were used to find the strain distribution on the strain-gauged board during sine sweep and dwell. That gave us a better understanding of how the board behaved

Table XIV
Vibration Test Result Summary, 5 G and 2 G

Batch number	Cards	Slot	T_g, °C	Alloy	Finish	Control G level	Resonance frequency, Hz	Card G level	Dwell frequency. Hz	Strain gauge 1		Strain gauge 12	
										Max., με	Min., με	Max., με	Min., με
1	R246010	B1	170	B	ENEPIG	5	48.61	45.499	52.66	236	−251	317	−181
	R239004	B2	170	A	ENIG		48.94	45.394					
	R248007	B3	170	SAC305	ENEPIG		55.92	51.523					
	R240008	B4	170	SnPb	ENEPIG		55.92	56.364					
2	R239009	B1	170	A	ENEPIG	5	...	...	54.81	218	−213	359	−114
	R240002	B2	170	SnPb	OSP		55.55	50.350					
3	R247007	B1	170	C	ENIG	5	62.22	63.387	60.99	178	−181	207	−114
	R246002	B2	170	B	OSP		55.92	59.704					
	R248002	B3	170	SAC305	OSP		60.18	66.069					
	R247002	B4	170	C	OSP		60.99	67.143					
4	R239008	B1	155	A	OSP	5	53.02	44.566	52.66	243	−258	262	−242
	R248005	B2	155	SAC305	OSP		52.66	46.666					
	R240006	B3	155	SnPb	OSP		49.59	50.816					
5	R246006	B1	155	B	ENIG	5	54.45	51.286	56.30	243	−254	2B2	−291
	R248009	B2	155	SAC305	ENEPIG		57.05	59.704					
	R240010	B3	155	SnPb	ENEPIG		56.67	63.533					
	R247010	B4	155	C	ENEPIG		52 66	54.450					
6	R239006	B1	155	A	OSP	2	57.82	41.687	57.82	No strain			
	R246008	B2	155	B	ENIG		47.97	28.973					
	R247011	B3	155	C	ENEPIG		59.38	52.966					
7	R239003	B1	170	A	ENIG	2	57.43	30.620	56.67	No strain			
	R246011	B2	170	B	ENEPIG		48.61	25.645					
	R247004	B3	170	C	OSP		58.99	36.308					
8	R239010	B1	170	A	ENEPIG	2	48.94	31.915	48.94	No strain			
	R246001	B2	170	B	OSP		54.45	38.282					
	R247008	B3	170	C	ENIG		49.59	32.961					

Table XV
Maximum Strain Values at 5 Gpk Sine Sweep

	Strain gauges and their channel numbers									
	CH1	CH2	CH3	CH(4-6)		CH(7-9)		CH10	CH11	CH12
Batch	Max., με	Max., με	Max., με	Max., με	Min., με	Max., με	Min., με	Max., με	Max., με	Max., με
1	236	176	168	146	−66	135	−50	152	120	317
2	218	108	37	87	−73	94	−78	82	127	359
3	178	111	187	117	−46	106	−60	157	123	207
4	243	136	0	92	−79	103	−98	−14	81	262
5	243	134	61	103	−96	123	−96	75	161	282

during the test and gave us a good picture of strain levels of each component during the test. The test results confirmed that the maximum strain happens at the resonance frequency of the card. Then the maximum strain value of each location was determined; maximum strain values are listed in Table XV. The linear strain gauges measure the strain in one direction and the maximum value calculations for linear strain gauges are straightforward. The rosette strain gauges measure the strain in three directions. Two readings are in orthogonal directions and the third one is 45° to the other two, and the maximum and minimum principal strains are calculated using those three readings.

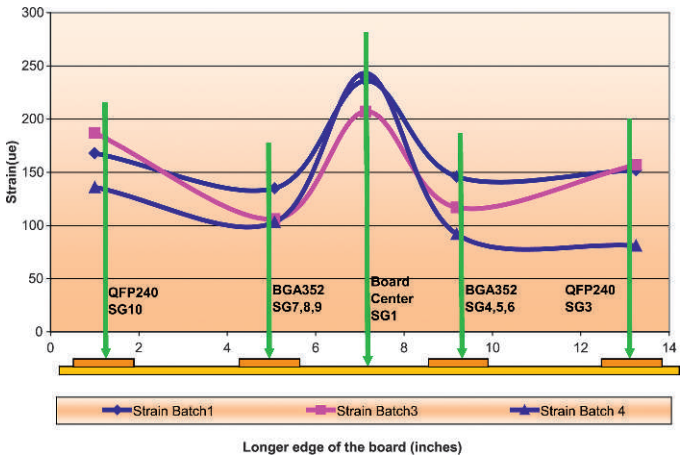

Fig. 41. Strain distribution along longer edge of board.

Maximum strain occurred at the center of the board and strain values decreased with a nonlinear pattern when the strain measurement point moved away from the center, as shown in Fig. 41. These strain distribution results confirm that the cards resonated at their first mode natural frequency. We found this strain distribution result is similar to the NASA–DoD Pb-free project strain distribution results [18, 19].

A general strain value behavior noted was that the strain value was at its maximum when the dwell started, then it decreased with dwell time. The cards' deflections were high at the beginning of the dwell, since the dwell frequency was very close to the cards' resonance frequency at that stage. The formation and accumulation of laminate and/or solder defects changes the stiffness, therefore changing the resonance of the

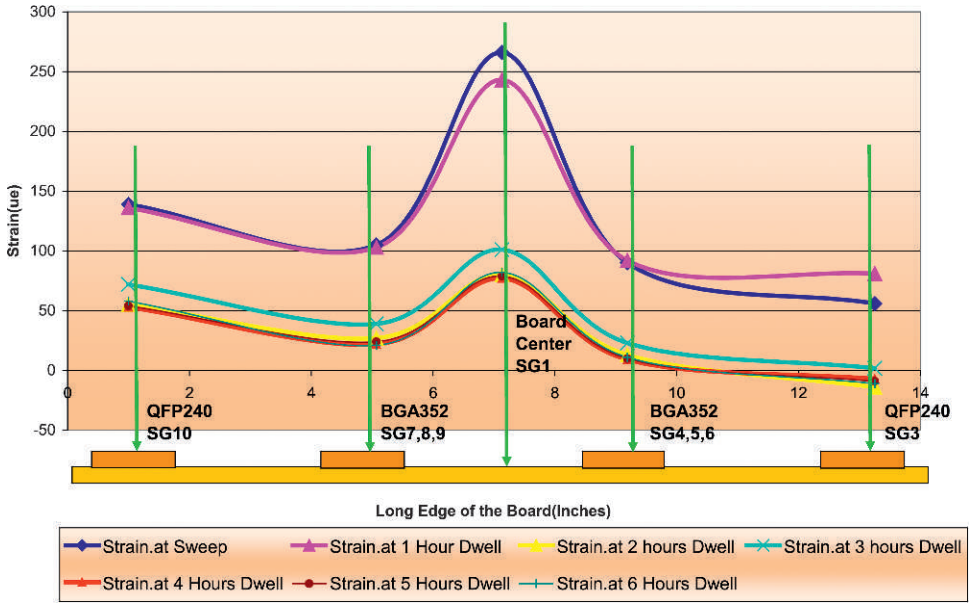

Fig. 42. Strain distribution change on components during 6-h dwell.

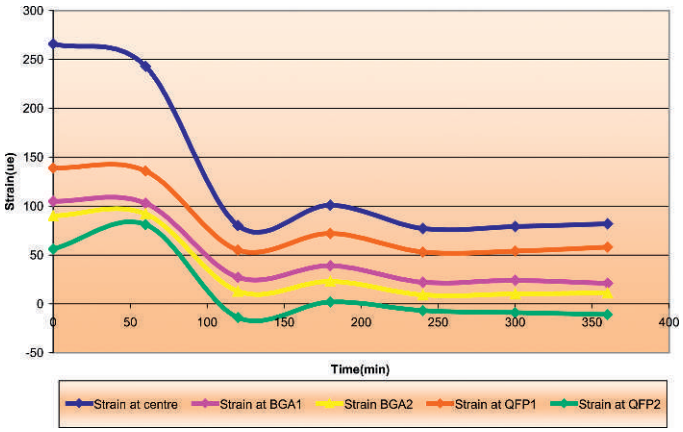

Fig. 43. Typical strain versus time graph during sine sweep on components.

test sample. The dwell frequency was maintained consistent throughout the 6-h dwell, so the card deflection must have decreased over the dwell time and resulted in a decrease in strain, as seen in Fig. 42.

As Fig. 43 indicates, all components' strain values follow a steep downward pattern from the start of the test to just before the 2-h mark. From this point forward, strain values appear to remain fairly consistent on a flat line.

E. Strain Distribution on the Samples at Resonance Frequency

The strain graphs indicate that the strain level of the sample increased with the frequency during the sweep and reached the maximum when the card experienced the resonance frequency. Strain gauge 1 location is at the component-side center of the test sample and strain gauge 12 location is at the bottom-side center of the test vehicle; theoretically, these locations' strain readings should be equal if the conditions on both sides of the board are the same. In our experiment, channel 12 on the bottom of the board displayed a slightly higher strain than channel 1 on the component side, because the components provided local stiffening in their respective regions and, as a result, created a global stiffening effect on the component side of the card. The testing revealed that the theoretical expectation is correct and the testing methodology is correct.

Fig. 44 shows the 5-G sweep strain data for channel 1. The test frequency range is 10-200 Hz at a rate of 1 octave/min and total duration of 4.18 min. As the vibration begins, the test vehicle deflection starts to increase, and that causes the strain to increase. Due to this proportional relationship

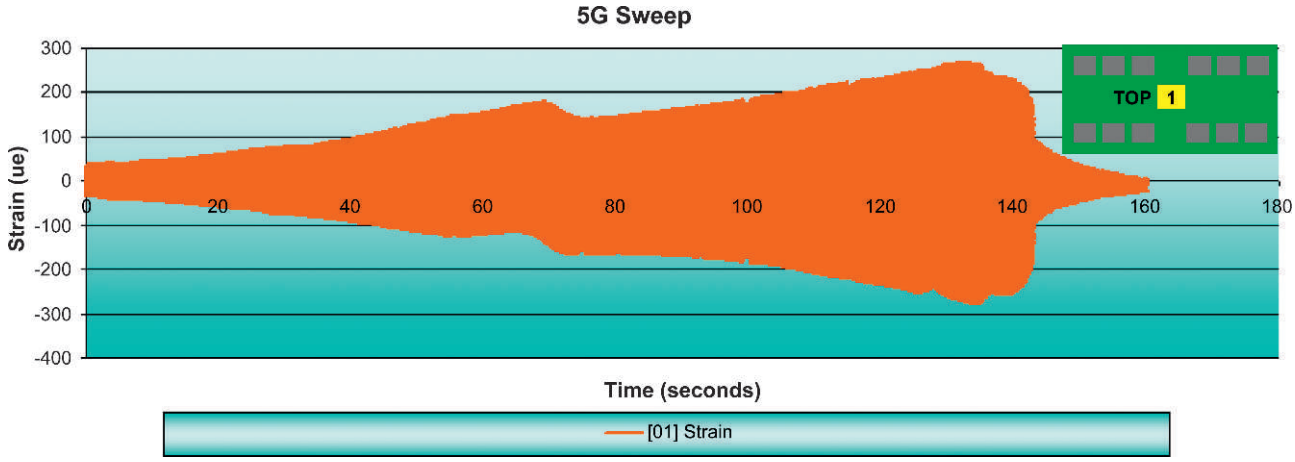

Fig. 44. Strain at 5-G sine sweep on channel 1.

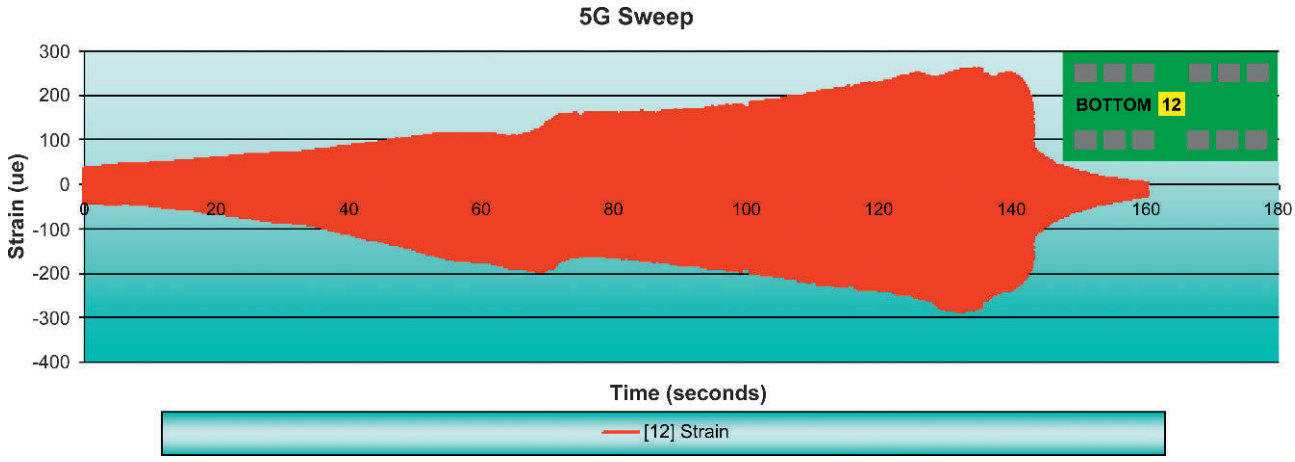

Fig. 45. Strain at 5-G sine sweep on channel 12.

between strain and displacement, both increased to a maximum value until the resonance frequency occurred at 48.61 Hz, which happened 136.9 s from the sweep start. All the sweep strain data were collected, but the strain graph was plotted only for 2.67 min, since no valuable strain event occurred beyond this point. Similar data are shown in Fig. 45 for Channel 12.

F. Vibration Resistance Measurement Details

The intent of the design of the experimental runs listed in Table XVI was to compare the several combinations of solder paste, substrate finish, and T_g; two designed experimental matrices were chosen using a full factorial for the baseline tin-lead and SAC305, and a Latin square for the low melt products (Table VI).

The Latin square design of order 3 was shown in Table V and Table VI. In general, the rows represent levels of one factor; the columns, another factor; and numbers in the cells, levels of a third factor. The Latin square is a subset of all possible combinations, where each level of one factor is present with each level of another factor. The advantage is that the Latin square provides estimates of factor level differences in a fraction of the possible combinations. In this case, the Latin square of order 3 uses nine combinations rather than the 27 required for a full factorial experiment [13].

The run data were summarized as pass/fail for each component and are shown in Table XVI. Most of the BGAs and QFPs failed within the first 2 h of 5-G dwell. Component PLCC84 had some failures during the 5-G dwell, and component SSOP48 had fewer failures.

The initial analysis intent was to use the time to failure as a variable Y (either an estimate of mean time between failures or time to first failure in the group). This would have been an analysis of variance to look for any main effects that work consistently across the levels of the other factors. Because we only ran for only approximately 1 million cycles, several parts did not fail, limiting the variable analysis. The use of the fraction failing in each group was a possibility, but it did not give us much to work, with since the number of samples was small.

The analysis is mainly an inspection of the cube plots with the third factor as the point color, using Minitab 16. Since we were really looking for a potential combination of paste and finish that worked across components (and, to a certain extent, T_g), the data are not so much an analytical conclusion with statistical calculations as an elimination of the obvious (i.e., the near-impossible possibilities) to find the area for the next experiment. Essentially, this experiment was a screening experiment. To this end, in Fig. 46, the results of the full factorial show the combination OSP, SnPb, and T_g of 155°C to be the most robust for the component types PLCC84, BGA352, QFP240, and SSOP48. For the SSOP48, however, all combinations worked well except OSP/SAC305 with T_g of 170°C. In Fig. 47, the results of the Latin squares, shown in circles in the figure, indicate the combination OSP/Violet and T_g of 170°C was the most robust for the component types PLCC84, BGA352, QFP240, and SSOP48.

Failure data also exist for the 2-G harmonic vibration. Table XVII lists the results for 48 components each for Paul, Violet, and Orchid solders, with no failures in BGAs and SSOPs. Considering all of the components, Violet had two combinations where all the components survived, Paul had one combination where all components survived, and Orchid had none. In Fig. 48, observe that when the 5-G and 2-G harmonics are juxtaposed, the survival trend stays intact; namely, Violet survives the longest, then Paul, then Orchid. This is the same trend that was observed in 5-G testing. Furthermore, the Paul and Violet pastes in the 5-G environment acted more like the SnPb solder paste and less like the SAC305, which showed higher failures.

Table XVI
Resistance Monitoring Failure Details for 5-G Test

Card No.	R239008	R239004	R239009	R246002	R246006	R246010	R247002	R247007	R247010
Paste type	Paul			Violet			Orchid		
Finish	OSP	ENIG	ENEPIG	OSP	ENIG	ENEPIG	OSP	ENIG	ENEPIG
T_g, °C	155	170	170	170	155	170	170	170	155
Component Type									
BGA352	02/02	02/02	01/02	00/02	02/02	02/02	02/02	02/02	01/02
QFP240	02/02	02/02	02/02	00/02	02/02	02/02	02/02	02/02	02/02
SSOP48	00/06	02/06	00/06	00/06	00/06	00/06	01/06	02/06	00/06
PLCC84	01/06	04/06	00/06	00/06	01/06	05/06	01/06	02/06	04/06

Card No.	R248005	R248002	R248009	R248007	R240006	R240002	R240010	R240008
Paste type	SAC305				SnPb			
Finish	OSP	OSP	ENEPIG	ENEPIG	OSP	OSP	ENEPIG	ENEPIG
T_g, °C	155	170	155	170	155	170	155	170
Component Type								
BGA352	02/02	02/02	02/02	02/02	00/02	02/02	00/02	02/02
QFP240	02/02	02/02	02/02	02/02	00/02	02/02	02/02	02/02
SSOP48	00/06	01/06	00/06	00/06	00/06	00/06	00/06	00/06
PLCC84	03/06	04/06	04/06	03/06	00/06	03/06	04/06	06/06

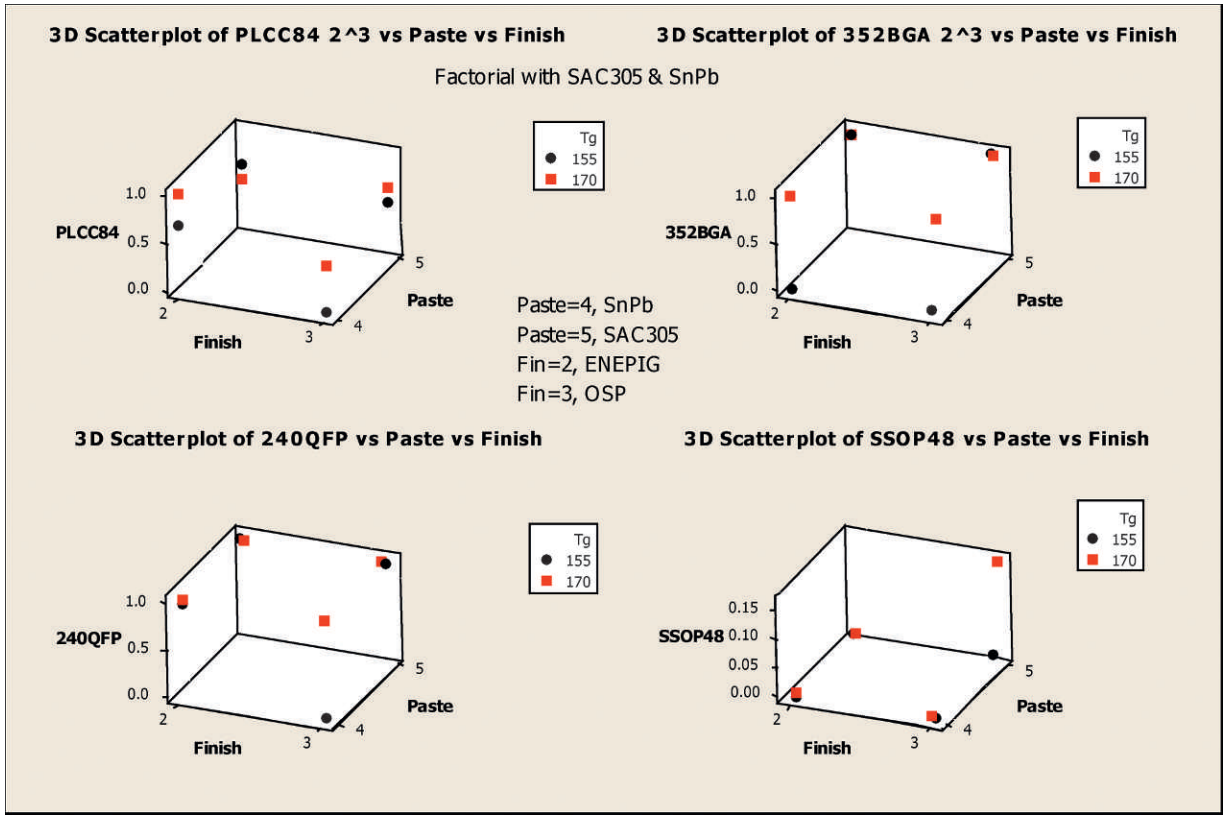

Fig. 46. 3-D scatter plots for SnPb and SAC305 solder paste, finish, and T_g versus percentage failed at 5-G harmonic dwell at first resonance frequency [20].

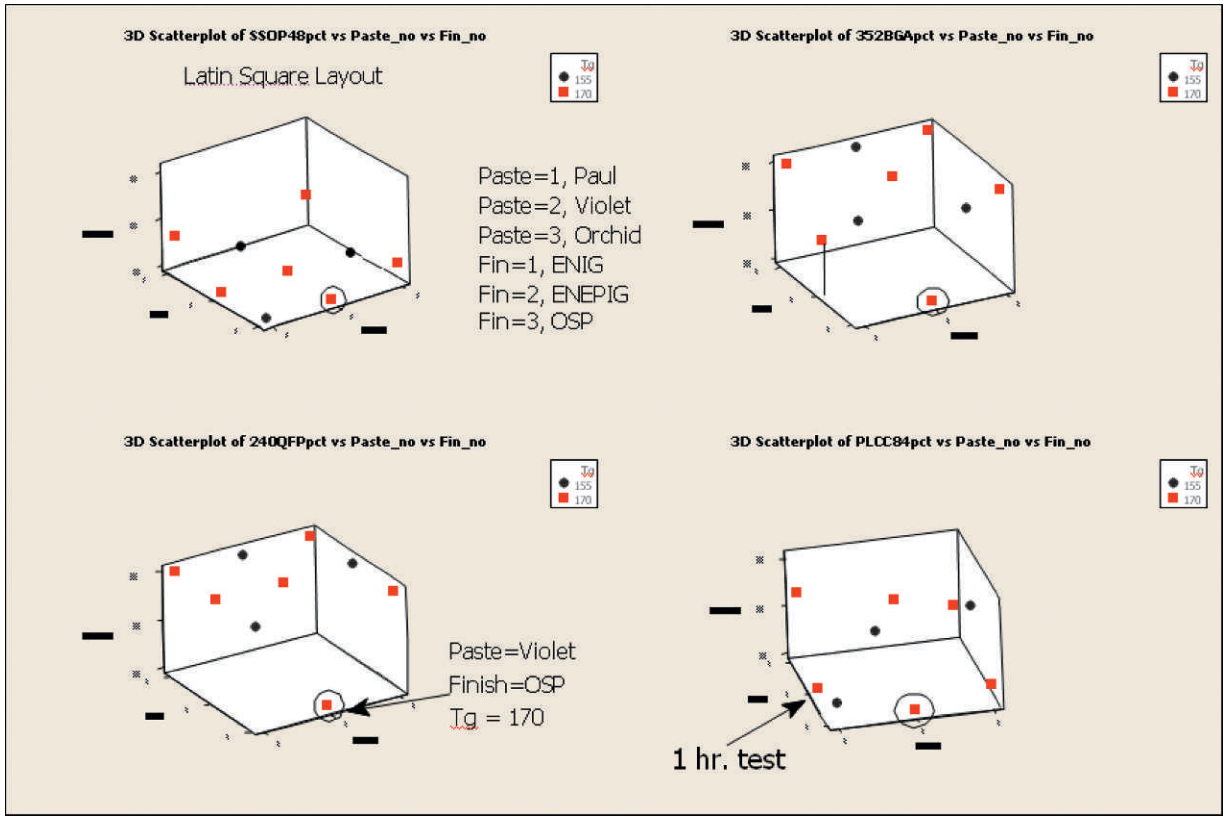

Fig. 47. 3-D scatter plots for solder paste, finish, and T_g versus percentage failed at 5-G harmonic dwell at first resonance frequency [20].

Table XVII
Resistance Monitoring Failure Details for 2-G Test

Card No.	R239006	R239003	R239010	R246001	R246008	R246011	R247004	R247008	R247011
Paste type		Paul			Violet			Orchid	
Finish	OSP	ENIG	ENEPIG	OSP	ENIG	ENEPIG	OSP	ENIG	ENEPIG
T_g, °C	155	170	170	170	155	170	170	170	155
Component type									
BGA352	00/02	00/02	00/02	00/02	00/02	00/02	00/02	00/02	00/02
QFP240	02/02	00/02	00/02	00/02	02/02	00/02	02/02	02/02	01/02
SSOP48	00/06	00/06	00/06	00/06	00/06	00/06	00/06	00/06	00/06
PLCC84	01/06	00/06	02/06	00/06	00/06	00/06	00/06	04/06	00/06

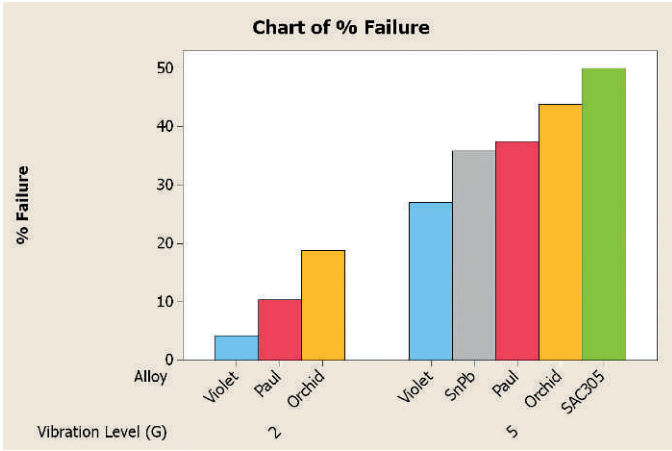

Fig. 48. Percent failed components: BGA352, QFP240, SSOP48, and PLCC84 after 6-h dwell at 2-G and 5-G vibration.

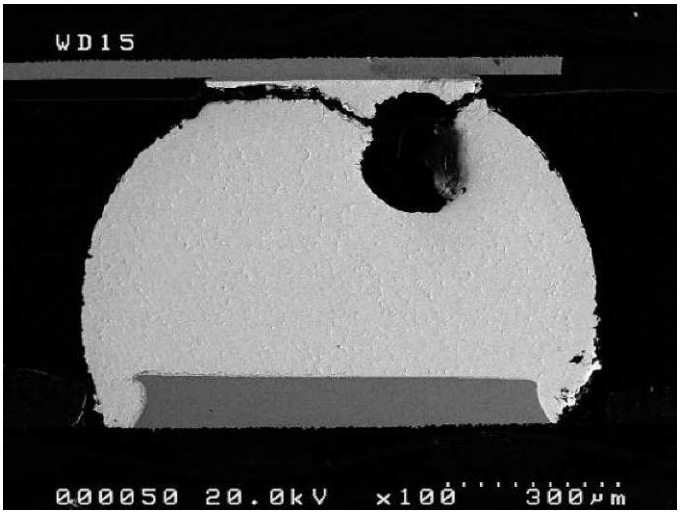

Fig. 49. BGA with SAC305 on ENEPIG finish, 170°C T_g board.

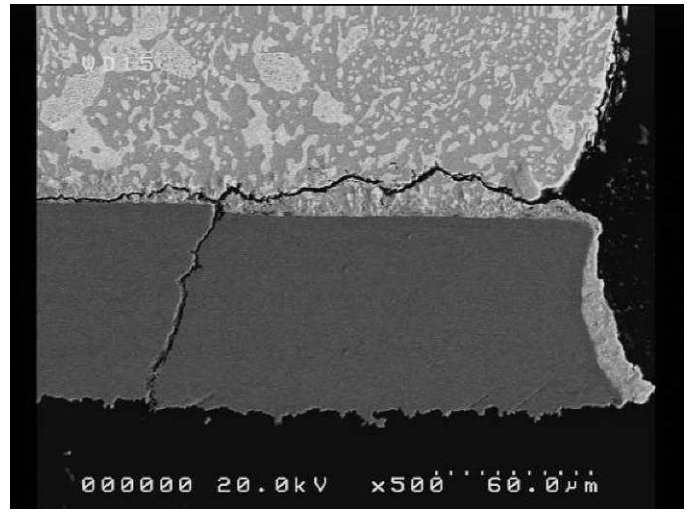

Fig. 50. BGA with SnPb on ENEPIG finish, 170°C T_g board.

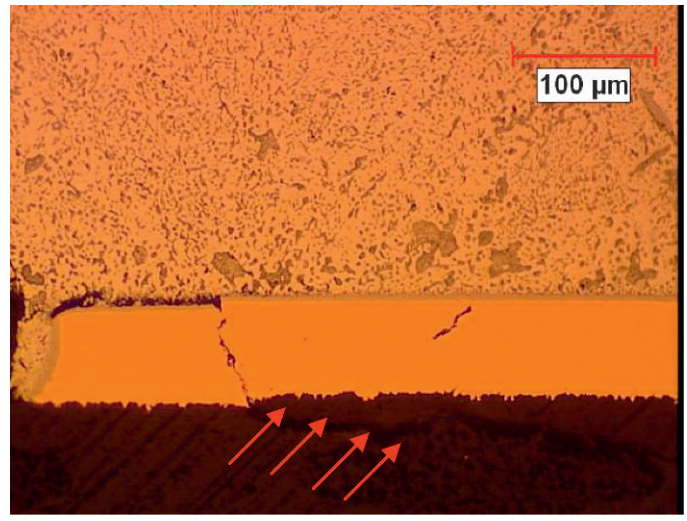

Fig. 51. Board side failure (with pad crater) of BGA with SnPb solder on ENEPIG finish (170°C T_g board).

G. Metallurgical Analysis After Vibration Testing

Failure analysis focused on four component types: BGA352, QFP240, SSOP48, and PLCC84.

There was no BGA failure after 2-G vibration. Twenty percent of BGAs assembled on 155°C T_g boards and 82.2% of BGAs assembled on 170°C T_g boards failed after 5-G vibration. Typically, the BGAs failed through the solder either at the component side, as illustrated in Fig. 49, or closer to the board side, in which case the copper pad was also damaged, as illustrated in Fig. 50.

The board material had a noticeable impact on the failure modes; 170°C T_g and, in some cases, 155°C board materials experienced failure via pad cratering, as seen in Fig. 51. This failure occurred at locations where the copper pad had cracked through. The 155°C T_g boards had failures in the vias in the form of barrel cracks.

Surface finish also had an impact on the failure mode: All BGA failures on boards with OSP finish occurred through the solder, as illustrated in Fig. 52. ENEPIG failures occurred mainly in the same fashion, through the solder, as shown in Fig. 53 and Fig. 54, with the exception of those failures that occurred with Orchid solder paste on ENEPIG finished boards. As shown in Fig. 55, these failed through the brittle IMC layer formed between the solder and the board-side copper pad with ENEPIG finish. All ENIG failures resulted from separation of the IMC from the board, as shown in Fig. 56.

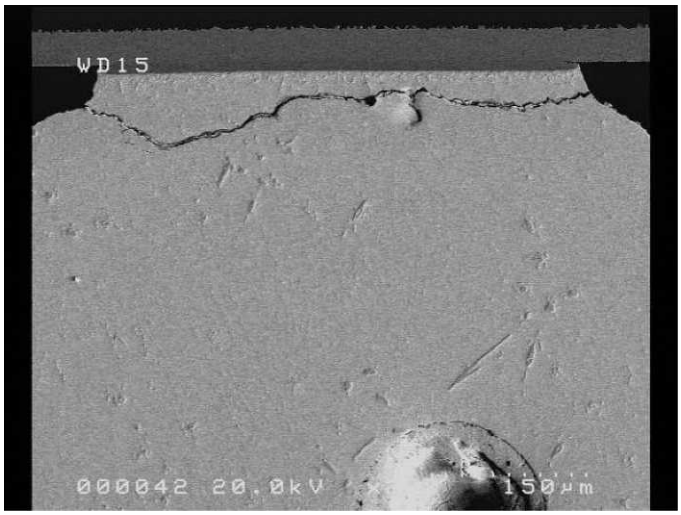

Fig. 52. Component side failure with SAC305 solder on OSP finish (170°C T_g board).

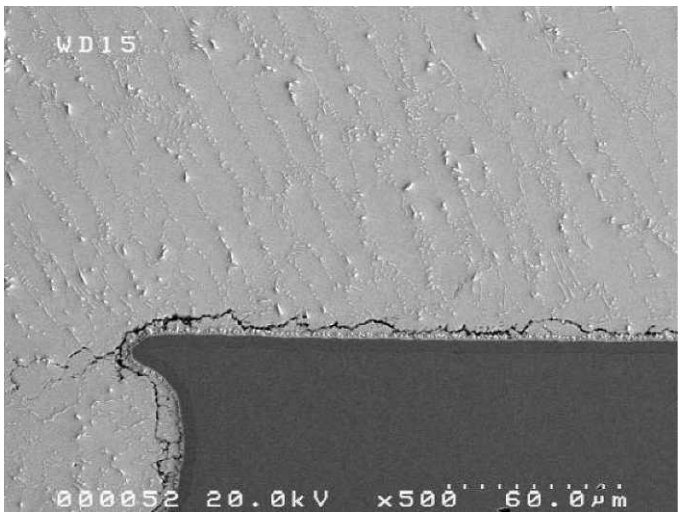

Fig. 53. Board side failure of BGA with SAC305 solder on ENEPIG finish (170°C T_g board), × 500 magnification.

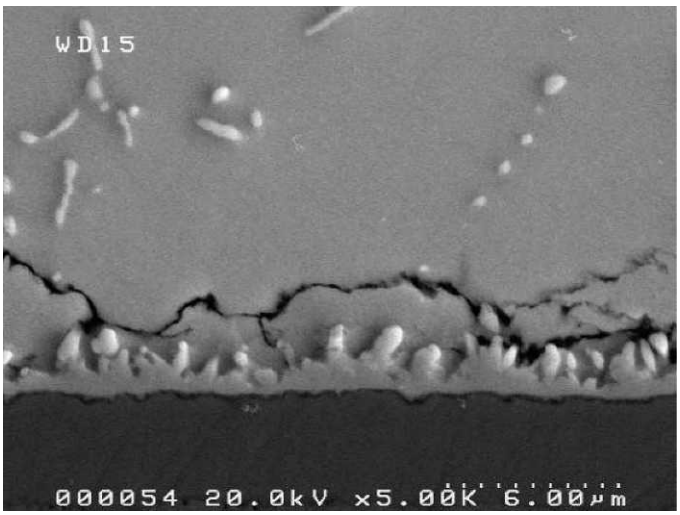

Fig. 54. Board side failure of BGA with SAC305 solder on ENEPIG finish (170°C T_g board), × 5,000 magnification.

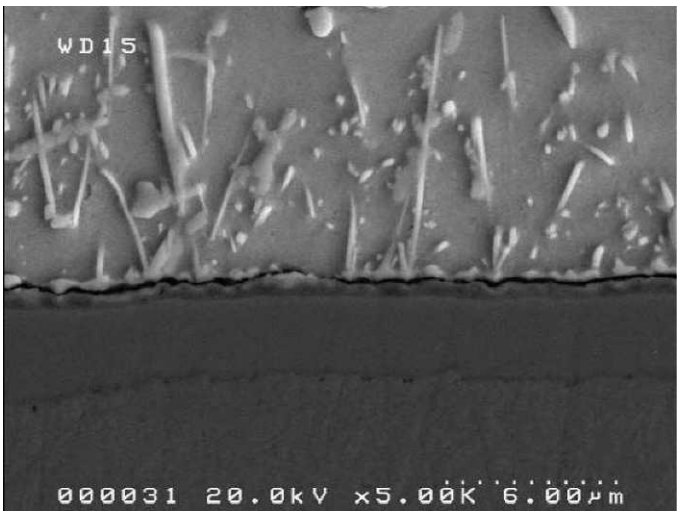

Fig. 55. Board side failure of BGA with Orchid solder on ENEPIG finish (170°C T_g board).

No failures occurred with Violet solder paste on OSP board finish. This solder–finish combination performed as well as SnPb on OSP and outperformed all other variations. Cross sections of this sample revealed good microstructural properties, with a consistent, unbroken IMC layer, as seen in Fig. 57 and Fig. 58.

QFP failures could be attributed to full cracks and breaks of the lead, as revealed in Fig. 59. The solder, however, appeared to be a factor, as the crack initiation appeared to occur within the solder along the lead, as shown in Fig. 60. Only Violet and SnPb solders appeared to have survived. No pad-crater mode was detected in QFP solder joints nor in 170°C or 155°C T_g boards. There was no difference in survival rate of QFPs assembled on 170°C and 155°C T_g boards, as well. The pad-crater failure mode is very typical for BGAs. There was a significant difference in survival rate between the BGAs assembled on 170°C and 155°C T_g boards. Eighty percent of

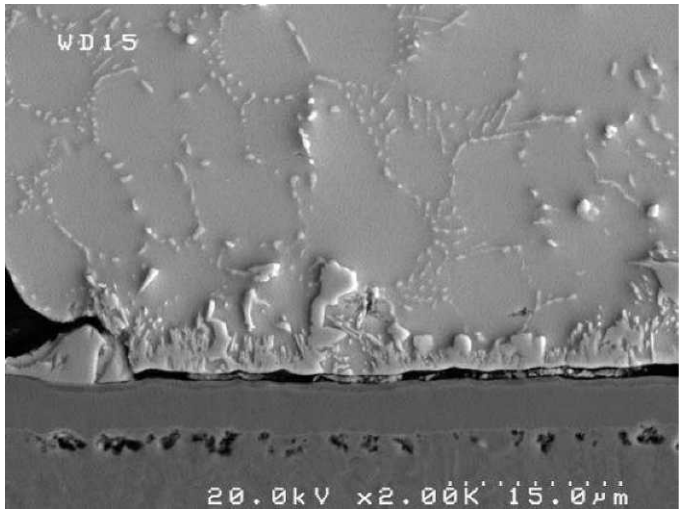

Fig. 56. Board side failure of BGA with Paul solder on ENIG finish (170°C T_g board).

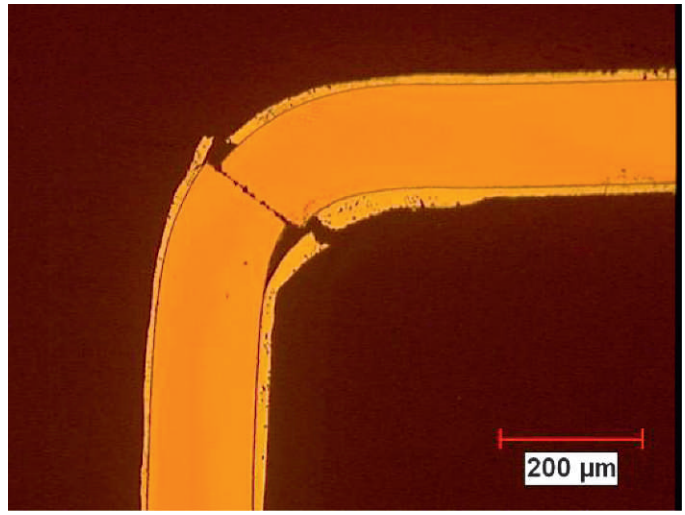

Fig. 59. QFP failure by broken lead.

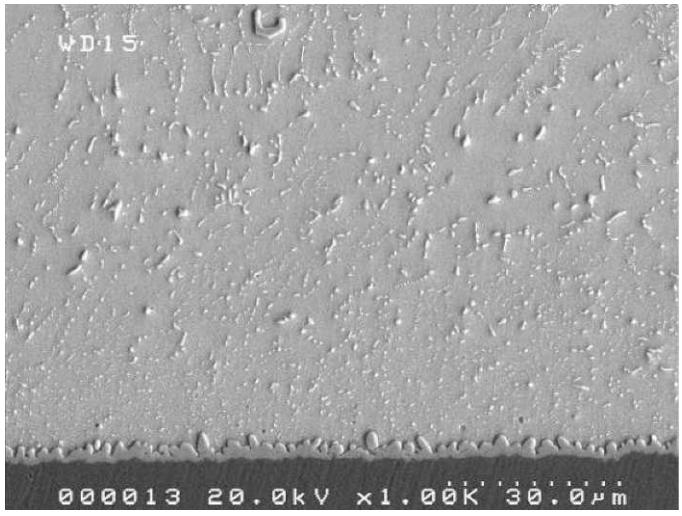

Fig. 57. BGA with Violet solder paste on OSP finish, × 1,000 magnification.

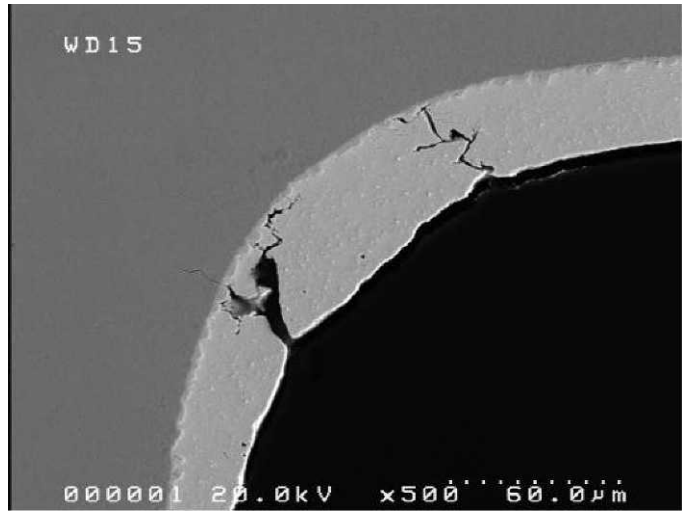

Fig. 60. QFP failure initiating in solder.

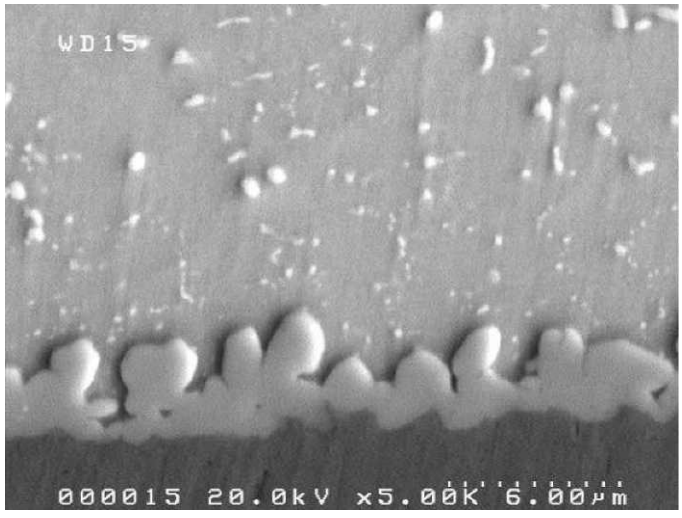

Fig. 58. BGA with Violet solder paste on OSP finish, × 5,000 magnification.

BGAs assembled on 155°C T_g boards using Paul, Violet, Orchid, and SnPb (SAC305 was excluded because 155°C T_g boards cannot be used for 240°C assembly) survived 1 million cycles at 5 G. Only 18.8% of the BGAs assembled using the same solder pastes on 170°C T_g boards survived 1 million cycles at 5 G. This suggests that the 155°C T_g laminate demonstrates a trend to pad-crater failure mode reduction.

Summary and Conclusions

The following results and conclusions are based on the results of the screening experiments on the manufacturability and reliability of lower melting, Pb-free alloys, which may be suitable for aerospace requirements.

Three Bi-containing alloys—Sn3.4Ag4.8Bi (Paul) and two reduced Ag-content variations, with and without Cu, Sn2.25Ag 0.5Cu6Bi (Violet) and Sn2Ag7Bi (Orchid)—were selected. Honeywell test vehicles were assembled using these alloys with

processing temperatures about 10°C below that for SAC305. Two board materials with high T_g (170°C) and normal T_g (155°C) were used. The boards were finished with OSP, ENIG, and ENEPIG. No problems related to the manufacturability were detected. Experimental alloys had better wetting and less voiding than SAC305. The joints were properly formed and were comparable to both SnPb and SAC305 joints.

The microstructural analysis after assembly revealed that

- All three Bi-containing alloys formed excellent joints on OSP finish. The interfacial intermetallic layer was comparable to SnPb in thickness and shape, and thinner than in SAC305.
- Sn3.4Ag4.8Bi (Paul) and Sn2Ag7Bi (Orchid) were not fully compatible with ENIG and ENEPIG, forming irregular and/or thicker interfacial intermetallic than SAC305. This is attributed to the lack of Cu in these alloy compositions.
- The alloy with Cu, Sn2.25Ag0.5Cu6Bi (Violet), is compatible not only with OSP but also with ENIG and ENEPIG, and forms excellent solder joints with uniform intermetallic layers on both BGA and leaded components.
- On the ENEPIG finish, Pd-containing, needle-shaped intermetallic particles were present in solder joints. These particles may cause solder joint embrittlement. The ENEPIG finish must be fully qualified for aerospace industry acceptance.

All combinations of alloys (Paul, Violet, Orchid, SAC305, and SnPb), surface finishes (OSP, ENIG, and ENEPIG), and board laminate (normal and high T_g) passed the aerospace ATC qualification requirement of 1,000 cycles of −55°C to 125°C. There was no solder joint failure on both high and normal T_g boards up to 3,010 cycles for Pb-free lower melt and SAC305 alloys. However, there were via failures in normal T_g boards with OSP finish assembled using all Pb-free and SnPb solders. Of these via failures on normal T_g OSP-finished boards, only the SAC305 cell did not meet the aerospace qualification requirement of 1,000 cycles. All three experimental alloys (i.e., Paul, Violet, and Orchid) showed excellent performance in harsh-environment thermal cycling.

An exceptional influence of bismuth additions on microstructural changes during thermal cycling was observed. Bi particles evenly precipitate in the tin matrix and reduce microstructure degradation.

The vibration failure results are based on 1 million cycles and show failure modes that might give an indication of what material combinations fail early. These observations for high-reliability products are important benchmarks. Both 2-G and 5-G vibration levels showed a similar failure progression of the number of failures based on resistance measurements. The order of the failure stayed the same. The lowest failure rate found was for Violet, followed by Paul and Orchid at the 2-G level. Violet and Paul showed the lowest rate of failure at the 5-G level, followed by SnPb and Orchid. The SAC305 had the highest failure rate. Our recommendation for future work would be to start at 5 G and then to select the higher G level that would precipitate more representative failure modes for the given amount of test time. Paul and Violet responded more like SnPb than SAC305, and thus appear to be a consistent, lower melt, robust substitute for SnPb.

The failure mode of QFPs in vibration testing was full cracking of the copper leads, which was observed to have initiated in the solder that wicked up along the lead during reflow. BGAs failed in vibration most frequently due to cracking through the bulk solder and laminate material, creating some degree of pad cratering. The cracks from the laminate material may propagate through the copper pad to the solder material, resulting in open joints. The 155°C T_g laminate material demonstrated a trend to pad-cratering reduction compared with the 170°C T_g material. Both ENIG and ENEPIG finishes showed failures at the IMC; ENEPIG exhibited failure through the brittle IMC formed with Orchid solder pastes, whereas ENIG resulted in failure between the IMC and copper pad with all alloys.

These screening experiments provide some insight into the main effects of the alloy performance and show positive evidence for future study. Based on the results of the screening experiments, the lower melting alloys containing bismuth, particularly Violet and Paul, are recommended for further statistically valid reliability testing. The recommended testing will enable the choice of an alternative RoHS Pb-free alloy with lower process temperature and better thermo-mechanical properties.

Acknowledgments

The authors thank the following individuals from Celestica: Russell Brush, Alon Walk, Kangwon Lee, and Veseyathaas Thambipillai for ATC testing and data analysis; Jie Qian for sample preparation; Jose Traya and Michael Emery for test vehicle assembly; Suthakaran Subramaniam and Michelle Le for vibration testing; and Dr. John Vic Grice, Honeywell Corporate consulting statistician, who helped design the experimental matrix.

References

[1] NASA-DoD Lead-Free Electronics Project Joint Test Report - Final December 2011 (NASA-DOD Lead-Free Electronics Project 2). Project Number: NT.1504, Technology Evaluation for Environmental Risk Mitigation Principal Center.

[2] P. Vianco and J. A. Regent, "Properties of ternary Sn-Ag-Bi solder alloys: part 1- thermal properties and microstructure analysis," *Journal of Electronic Materials*, Vol. 28, pp. 1127-1137, 1999.

[3] P. Vianco and J. A. Regent, "Properties of ternary Sn-Ag-Bi solder alloys: part 2- wettability and mechanical properties analysis," *Journal of Electronic Materials*, Vol. 28, No. 10, pp. 1138-1143, 1999.

[4] D. Witkin, "Creep behavior of Bi-containing lead-free solder alloys," *Journal of Electronic Materials*, Vol. 41, No. 2, pp. 190-203, 2012.

[5] E. Bradley, C. A. Handwerker, J. Bath, R. D. Parker, and R. W. Gedney, *Lead-Free Electronics: iNEMI Projects Lead to Successful Manufacturing*, Wiley-IEEE Press, Hoboken, NJ, 2007.

[6] NCMS, "Lead-free, high-temperature, fatigue-resistant solder: final report," National Center for Manufacturing Science, Ann Arbor, MI, 2001.

[7] Lead-Free Solder Testing for High Reliability (Project 1), Project Number: NT-1501, NASA John F. Kennedy Space Center, Technology Evaluation For Environmental Risk Mitigation (TEERM) Principal Center, 2006.

[8] G. Reichelt, "Conception and Production of high reliable PWB-assemblies for thermally and mechanically highly stressed long term reliable lead free electronic systems for Aeronautics," German Joint Project. Member presentation to PERM # 8, Noordwijk, Netherlands, 2011.

[9] P. Snugovsky, S. Bagheri, M. Romansky, D. Perovic, L. Snugovsky, and J. Rutter, "New generation of lead-free solder alloys: possible solution to solve current issues with main stream lead-free soldering," *SMTA Journal*, Vol. 25, 2012.

[10] J. M. Juarez, Jr., M. Robinson, J. Heebink, P. Snugovsky, E. Kosiba, J. Kennedy, Z. Bagheri, S. Suthakaran, and M. Romansky, "Reliability screening of lower melting point Pb-free alloys containing Bi [second paper in this series]," Proceedings of the IPC APEX EXPO Conference, 2014.
[11] E. Kosiba, S. Bagheri, Z. Bagheri, P. Snugovsky, and D. Perovic, "Assembly feasibility and property evaluation of new low melt solder alloys," Proceedings of ICSR SMTA, Toronto, 2012.
[12] D. C. Montgomery, *Design and Analysis of Experiments*, 7th ed, John Wiley & Sons, Hoboken, NJ, 2009.
[13] P. J. T. L. Oberndorff, "Lead-free solder systems: phase relations and microstructures," PhD thesis, Techische Universiteit Eindhoven, the Netherlands, 2001.
[14] L. Snugovsky, P. Snugovsky, D. D. Perovic, and J. W. Rutter, "Phase equilibria in the Sn-rich corner of the Cu-Ni-Sn system," *Materials Science and Technology*, Vol. 29, No. 8, pp. 899-902, 2006.
[15] C. E. Ho, S. C. Yang, and C. R. Kao, "Interfacial reaction issues for lead-free electronic solders," *Journal of Materials Science*, Vol. 18, pp. 155-174, 2007.
[16] Ronald E. Pratt, Eric I. Stromswold, and D. J. Quesnel, "Effect of solid-state intermetallic growth on the fracture toughness of Cu/63Sn-37Pb solder joints," *IEEE Transactions on Components Packaging & Manufacturing Technology Part A*, Vol. 19, No. 1, pp. 134-141, 1996.
[17] P. Snugovsky, E. Kosiba, J. Kennedy, Z. Bagheri, M. Romansky, M. Robinson, J. M. Juarez Jr., and J. Heebink, "Manufacturability and reliability screening of lower melting point Pb-free alloys containing Bi [first paper in this series]," Proceedings of the IPC APEX EXPO Conference, San Diego, CA, 2013.
[18] T. A. Woodrow, "NASA-DoD Lead-Free Electronics Project: vibration test," Boeing Electronics Materials and Processes Report - 603, June 30, 2010.
[19] NASA-DoD Lead-Free Electronics Project Plan, August 2009.
[20] Minitab 16 Statistical Software, www.minitab.com.